J. Mech. Phys. Solids 166 (2022) 104926

Contents lists available at ScienceDirect

Journal of the Mechanics and Physics of Solids

journal homepage: www.elsevier.com/locate/jmps

The arrest and recession dynamics of a deflating radial hydraulic fracture in a permeable elastic medium

Anthony Peirce

Department of Mathematics, The University of British Columbia, Vancouver, BC, Canada V6T 1Z2

ARTICLE INFO

Keywords:
Radial hydraulic fracture deflation
Arrest and recession
Multiscale tip asymptotics

ABSTRACT

In this paper we describe the post injection deflation dynamics of a radially symmetric hydraulic fracture in a permeable elastic medium. Depending on the parameters of the problem, the fracture may arrest almost immediately after injection has ceased, or continue to propagate despite the fluid loss to the porous medium. After arrest the fracture continues to deflate while the stress intensity factor decreases to zero, after which it recedes until the fracture finally collapses. In order to establish rigorous numerical solutions to explore this deflation dynamics, we make use of recent research (Peirce and Detournay, 2021) that derived vertex asymptotes for the arrest and recession phases of the deflation process as well as multiscale asymptotic solutions that connect these vertex asymptotes: during arrest, through the arrest–recession transition, and during recession. If only vertex asymptotes are used to capture the arrest and recession, the solution exhibits jump discontinuities through this arrest–recession transition point. We describe how the multiscale asymptotes can be used to obtain a smooth solution valid through the arrest–recession transition. Significantly, after the arrest–recession transition, the jump-induced transients decay and the solutions using vertex asymptotes converge to those that use multiscale asymptotes. Thus unless it is important to obtain a smooth solution through the arrest–recession transition, a practical, and more efficient, approach would be to use an algorithm based solely on vertex asymptotes. We also provide numerical confirmation of the emergence, beyond the arrest–recession transition time, of the dominant balance used in the asymptotic analysis to establish the linear recession asymptote $\hat{w} \sim \hat{r}$. We present a novel scaling analysis to establish the characteristic power laws for the arrest time, arrest radius, arrest aperture, and the deflation time, in terms of two new dimensionless parameters, which make it possible to unify the power laws between the zero and finite toughness cases. These power laws show close agreement with those obtained by regression of the numerical results over a range of the dimensionless parameters. Numerical solutions are provided to illustrate the solution landscape in parameter space and the effect that each of the dimensionless parameters has on: the duration of the period of propagation after injection has ceased, the duration of the arrest period, and the time from the initiation of recession to collapse.

1. Introduction

Hydraulic fractures occur naturally during ice calving events in glaciers, the sudden draining of glacial lakes, the formation of magma-driven dykes and sills, and the failure of dams. Hydraulic fractures are also engineered by injecting a viscous fluid into rock to increase hydro-carbon recovery, for enhanced geothermal energy production, to remediate and dispose of waste water, for

E-mail address: peirce@math.ubc.ca.

https://doi.org/10.1016/j.jmps.2022.104926
Received 16 March 2022; Accepted 4 May 2022
Available online 19 May 2022

preconditioning and cave inducement in mining operations, and, at a smaller scale, to generate miniature hydraulic fractures that are propagated and then allowed to recede in order to measure the leak-off coefficient or to identify the closure pressure to determine the minimum *in situ* stress σ_0. Once injection is stopped the wellbore is shut-in by closing a valve, or the fracture is allowed to bleed causing flow-back of fluid into the wellbore, or fluid is actively pumped from the wellbore. In this paper we consider the deflation dynamics of a radial hydraulic fracture as it leaks fluid to the porous medium after shut-in. After shut-in, depending on the various parameters characterizing the system, including those controlling the fluid leak-off and the volume of injected fluid in the fracture at the time of shut-in, the hydraulic fracture may arrest almost immediately or may continue to propagate while the fluid pressure adjusts to the change in boundary condition at the wellbore. After arrest the fracture may continue to deflate without altering its footprint while the stress intensity factor decreases to zero. Once the stress intensity factor is zero the fracture starts to recede until the point of collapse.

Over the last five decades considerable research has been dedicated to building accurate models of propagating hydraulic fractures with the primary objective being to determine the fracture footprint at shut-in. Because of their one dimensional structure plane strain and radially symmetric models of hydraulic fracture dynamics have always played a central role in the pursuit of theoretical developments and analytic solutions. Since the formulation of some of the early models of hydraulic fractures propagating in a state of plane strain (see e.g. Khristianovic and Zheltov (1955)) there has been considerable progress in the development of models of hydraulic fracture propagation. The seminal paper by Spence and Sharp (1985) on self-similar solutions and the landmark paper (Desroches et al., 1994) identifying the tip asymptotics of viscosity dominated hydraulic fracture propagation stimulated intense research into the study of the tip asymptotics (Garagash and Detournay, 2000; Garagash, 2006; Detournay, 2004; Adachi and Detournay, 2008; Detournay, 2016) and analytic solutions (Savitski and Detournay, 2002; Dontsov, 2016, 2017) for hydraulic fracture propagation over the subsequent two decades. Radial hydraulic fracture solutions have been particularly useful in benchmarking numerical algorithms (Savitski and Detournay, 2002; Dontsov, 2016; Lecampion et al., 2013) and the provision of starting solutions for these algorithms on a scale that is sufficiently small to ensure that the conditions can be assumed to be locally isotropic. A milestone in the success of this analytic work was the precise confirmation of the viscous and toughness dominated radial analytic solutions in laboratory experiments on translucent solids (Bunger and Detournay, 2008). Because of the importance of the behaviour of the solution in the tip region, it transpired that the tip asymptotic solutions also provide an extremely useful tool to develop numerical algorithms that can provide highly accurate solutions on extremely coarse meshes (Peirce and Detournay, 2008). Indeed, the efficacy of this approach was clearly demonstrated in a collaborative study that evaluated a number of numerical algorithms (Lecampion et al., 2013) and benchmarked their relative accuracy against an analytic solution and compared their relative efficiency. This approach has been further developed (Madyarova, 2003; Peirce, 2015; Dontsov and Peirce, 2017) to incorporate multiscale tip asymptotics (Garagash et al., 2011; Dontsov and Peirce, 2015) associated with the competition between multiple physical processes that may be active at the fracture tip.

In contrast to the significant progress made in the modelling of propagating hydraulic fractures, there has, to our knowledge, been very little development of rigorous models of deflating hydraulic fractures both at arrest and during recession. Indeed, even the propagation of radial hydraulic fractures after shut-in has only recently been subjected to rigorous study (Mori and Lecampion, 2021). Existing models of hydraulic fracture recession have been purely numerical and based on implementing a minimum aperture constraint (Desroches and Thiercelin, 1993; Adachi et al., 2007; McClure and Horne, 2013; Mohammadnejad and Andrade, 2016; Zanganeh et al., 2017), whose arbitrarily chosen magnitude can affect the solution. Though laboratory experiments have reported further propagation after shut-in and recession after arrest, they are not sufficiently accurate to calibrate these aperture constraint models as they rely on monitoring active acoustic emissions to infer the fracture front positions (De Pater et al., 1996; van Dam et al., 2000). Moreover, due to the absence of a rigorous model of post shut-in arrest and recession, current practice in leak-off identification (Economides and Nolte, 2000; Nolte, 1979) assumes that the footprint of the hydraulic fracture during deflation remains the same as it was at the point of shut-in. There is thus a compelling need for a semi-analytic model that accounts for the receding tip asymptotics and captures the deflation dynamics of a hydraulic fracture during arrest and recession. This paper aims to address this issue for the case of a radially symmetric fracture that deflates and recedes due to tip fluid losses to the porous medium.

Recent research on deflating hydraulic fractures (Peirce and Detournay, 2022a) has established the arrest and recession vertex asymptotes as well as the multiscale asymptotic solutions that apply through the arrest–recession transition. In this paper, we detail specialized fixed point iterative schemes that are required to implement these multiscale tip asymptotes in numerical models. We demonstrate that the multiscale asymptotic solutions make it possible to traverse the arrest–recession transition without the jump discontinuities that are observed when only vertex asymptotes are used, and that the solutions that use multiscale and vertex asymptotes ultimately converge away from the transition point. Numerical experiments confirm the emergence during recession of the linear tip behaviour that was established by asymptotic analysis. Mori and Lecampion (2021) established power laws that characterize post shut-in arrest, which are different for the zero and finite toughness cases. However, we show that by introducing two new dimensionless parameters (the dimensionless shut-in time ω and the arrest regime parameter ϕ^V) it is possible to unify the scaling laws for the arrest time, the arrest radius, and the arrest aperture, which share the same exponents for both the zero and finite toughness cases. We also establish the first scaling law for the deflation time, which is also valid for both zero and finite toughness cases. Numerical results from a scheme that incorporates the multiscale tip asymptotes are used to confirm the scaling laws and to explore the impact of the dimensionless parameters ω and ϕ^V on the modes of arrest and recession. We also provide a solution in physical units for a parameter set that might be encountered in the field.

In Section 2, we describe the mathematical model for a radially symmetric fracture that can propagate, deflate, and recede in a porous elastic medium. In Section 3, we describe the tip asymptotic behaviour for propagating hydraulic fractures; describe the multiscale asymptotes for deflating hydraulic fractures through arrest, the arrest–recession transition, and during recession; detail

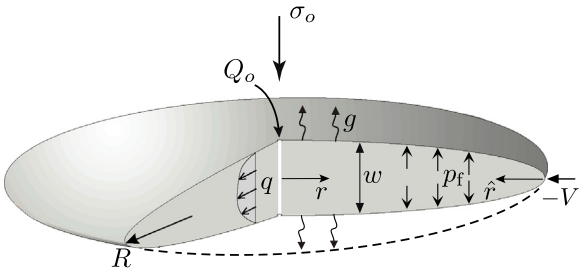

Fig. 1. Schematic showing the radial fracture geometry along with the coordinate systems used in the model.

specialized iterative schemes required to implement these multiscale asymptotes in a numerical algorithm; and demonstrate that the multiscale asymptotes are required to achieve smooth solutions through the arrest–recession transition point. In Section 4, we present a scaling analysis and introduce the pair of novel dimensionless parameters, which make it possible to unify the power laws that apply for both zero and finite toughness cases. In Section 5, we present numerical results that use the multiscale asymptotics to explore the impact of the dimensionless parameters on the time between shut-in and arrest, the duration of arrest, and the elapsed time from the initiation of arrest to collapse of the fracture. In Section 6, we make some concluding remarks.

2. Mathematical model

The mathematical model describing the dynamics of a fluid driven fracture needs to account for the dominant physical processes involved, such as: the deformation of the rock due to fracture opening; a mechanism for fracture growth; a description of the fluid-flow within the fracture; and the leak-off of fluid to the surrounding porous medium. In order that the model is tractable we make the following simplifying assumptions: the fracture propagates in a linear elastic solid characterized by Young's modulus E and Poisson's ratio ν; growth of the fracture is assumed to be mode I according to linear elastic fracture mechanics (LEFM) and is modulated by fracture toughness K_{Ic}; fluid-flow within the fracture is assumed to be laminar, follows lubrication theory, and the fluid is assumed to be incompressible and Newtonian with a dynamic viscosity μ; a uniform far-field stress field σ_0 acts normal to the fracture plane; leak-off is governed by Carter's model (Carter, 1957) characterized by the leak-off coefficient C_L; we assume that the fluid and fracture fronts coalesce; and the solid medium is assumed to be homogeneous so that E, ν, K_{Ic}, and C_L are all constant.

2.1. Governing equations for a radial hydraulic fracture in a permeable medium

Since the solid medium and external stress field are assumed to be homogeneous, the fracture will develop symmetrically about the injection point. Because there is no angular dependence, the radial coordinate $r \in (0, R)$ centred on the injection point completely defines the planar footprint of the circular fracture of radius $R(t)$ (see Fig. 1). The primary unknowns in a hydraulic fracture problem are the fracture aperture $w(r,t)$, the fluid pressure $p_f(r,t)$ or net pressure $p(r,t) = p_f(r,t) - \sigma_0$, and the fracture radius $R(t)$. The solution depends on the injection rate $Q(t)$ and the following four alternate material parameters that are introduced to keep formulae uncluttered by unnecessary constants: the plane strain modulus E', the alternate viscosity μ', the alternate fracture toughness K', and the alternate Carter leak-off coefficient C', defined by

$$E' = \frac{E}{1-\nu^2},\ \ \mu' = 12\mu,\ \ K' = \left(\frac{32}{\pi}\right)^{1/2} K_{Ic},\ \ C' = 2C_L \tag{1}$$

2.1.1. Elasticity

For a radial fracture with a radius R in an infinite, homogeneous, linear elastic solid, the relationship expressing the elastic equilibrium between the fracture aperture w and the imposed net pressure p, can be represented by an integral equation of the following form (Hills et al., 1996; Dontsov, 2016):

$$p(r,t) = -\frac{E'}{2\pi R(t)} \int_0^R M\left(\frac{r}{R}, \frac{r'}{R}\right) \frac{\partial w(r',t)}{\partial r'} dr' \tag{2}$$

where the kernel M is given by:

$$M(\rho, s) = \begin{cases} \frac{1}{\rho} K\left(\frac{s^2}{\rho^2}\right) + \frac{\rho}{s^2-\rho^2} E\left(\frac{s^2}{\rho^2}\right), & \rho > s \\ \frac{s}{s^2-\rho^2} E\left(\frac{s^2}{\rho^2}\right), & \rho < s \end{cases} \tag{3}$$

where $K(.)$ and $E(.)$ are complete elliptic integrals of the first and second kind.

Singularity structure of the elasticity kernel M and dominant tip behaviour: If we consider source points $s = \rho \pm \varepsilon$ a small distance ε either side of the receiving point ρ and expand the kernel function M given in (3), we observe that the dominant behaviour of M reduces to that of a Cauchy kernel

$$M(\rho, \rho \pm \varepsilon) = \pm\frac{1}{2\varepsilon} + O(\log(\varepsilon)) \sim \frac{1}{2(s-\rho)} \tag{4}$$

where the logarithmic and higher order terms will, upon integration over a finite interval, yield results that are finite.

In order to perform a local analysis to determine the behaviour of the solution in the vicinity of the fracture tip, it is convenient to introduce a new coordinate $\hat{r} = R(t) - r$ located on the moving tip and pointing inwards toward the injection point at the centre of the fracture (see Fig. 1). If we replace the kernel in (2) by the leading order Cauchy kernel, then the dominant part of the integral is left invariant under this transformation to the tip coordinate $\hat{r}$. To determine the dominant behaviour of the pressure field associated with an aperture that is a power law when expressed as a function of the distance to the tip, we will make use of the following integral (Peirce and Detournay, 2022b):

$$\int_0^a \frac{\hat{s}^\kappa}{\hat{s}-\hat{\rho}} d\hat{s} = \begin{cases} -\pi \cot(\pi\kappa)\hat{\rho}^\kappa + C, & -1 < \kappa \notin \mathbb{Z}^+ \\ -\hat{\rho}^\kappa \log \hat{\rho} + C, & \kappa \in \mathbb{Z}^+ \end{cases} \tag{5}$$

where $\mathbb{Z}^+ = \{0, 1, \ldots\}$ and C signifies that the next term is a constant.

2.1.2. Lubrication

By combining Poiseuille's law with the continuity equation adapted to account for fluid leak-off, we obtain the lubrication equation (Savitski and Detournay, 2002) relating $w(r,t)$ and $p(r,t)$:

$$\frac{\partial w}{\partial t} = \frac{1}{\mu' r}\frac{\partial}{\partial r}\left(r w^3 \frac{\partial p}{\partial r}\right) - g(r,t) + Q(t)\frac{\delta(r)}{2\pi r} \tag{6}$$

in which g is the Carter Leak-off term $g(r,t) = \frac{C'}{\sqrt{t-t_o(r)}}$, where $t_o(r)$ denotes the time of first exposure of point r to the fracturing fluid. The point source is represented by the δ-function in (6) and we will be considering a propagation phase during which the fluid is injected at a constant rate Q_0, followed by a shut-in phase initiated at time t_s, after which there is no further fluid injected into the fracture. The source function $Q(t)$ can therefore be written as

$$Q(t) = \begin{cases} Q_o & 0 < t < t_s \\ 0 & t \geq t_s \end{cases}$$

We note that the leak-off term g, which is singular at the tip during the propagation phase, becomes non-singular immediately after arrest, and evolves to a function that is more spatially homogeneous as deflation progresses.

Tip lubrication equation Introducing the tip unknowns $\hat{w}(\hat{r},t)$ and $\hat{p}(\hat{r},t)$, expressed in terms of the tip coordinate $\hat{r}$, the lubrication equation (6), defined on the interval $0 < \hat{r} < R(t)$, assumes the form:

$$\frac{\partial \hat{w}}{\partial t} + V\frac{\partial \hat{w}}{\partial \hat{r}} = \frac{1}{\mu'(R-\hat{r})}\frac{\partial}{\partial \hat{r}}\left((R-\hat{r})\hat{w}^3\frac{\partial \hat{p}}{\partial \hat{r}}\right) - \hat{g} \tag{7}$$

where $V = \dot{R}$ is the velocity of the tip.

2.1.3. Initial, boundary, and propagation conditions at the moving front $R(t)$

Initial conditions: The initial conditions are formally given by

$$R = 0, \quad w = 0, \quad p = 0, \quad \text{at } t = 0. \tag{8}$$

Boundary conditions: For coalescent fluid and fracture fronts the boundary conditions at the crack tip $r = R$ are that the fracture aperture and fluid flux are zero at the tip (Detournay and Peirce, 2014)

$$w = 0, \quad w^3\frac{\partial p}{\partial r} = 0, \quad \text{at } r = R. \tag{9}$$

Given these initial and boundary conditions, by integrating the lubrication equation (6) in both time and space we obtain the equation for the global volume balance:

$$\int_0^{R(t)} w(r,t)\, r\mathrm{d}r + 2C' \int_0^{R(t)} \sqrt{t - t_o(r)}\, r\mathrm{d}r = \frac{V_f(t)}{2\pi} \tag{10}$$

where

$$V_f = \begin{cases} Q_o t & 0 < t < t_s \\ V_s = Q_o t_s & t \geq t_s \end{cases}$$

This equation simply establishes that the total volume of fluid injected at time t is equal to the volume of fluid contained in the crack plus the total volume of fluid lost to the permeable rock.

Propagation condition: Since the fracture is assumed to propagate in limit equilibrium, LEFM (Rice, 1968) implies that the scaled mode-I stress intensity factor K satisfies the following inequality constraint:

$$K := E' \lim_{r\to R} \frac{w}{\sqrt{R-r}} = E' \lim_{\hat{r}\to 0} \frac{\hat{w}}{\sqrt{\hat{r}}} \le K' \tag{11}$$

Equality in (11) occurs when the fracture is propagating, i.e. $V > 0$, while strict inequality in (11) is associated with arrest characterized by $V = 0$, and recession characterized by $V < 0$ and $K' = 0$.

3. Tip asymptotics for a HF in a permeable medium

3.1. Local analysis and vertex asymptotes

Since we are interested in the behaviour of the solution near the tip, we assume power law asymptotic solutions of the form:

$$\hat{w} \overset{\hat{r}\to 0}{\sim} A(t)\hat{r}^{\alpha}, \ \frac{1}{2} \le \alpha \le 1, \tag{12}$$

Making use of (2)–(5) we obtain the following expression for the leading behaviour of the tip pressure

$$\hat{p} \overset{\hat{r}\to 0}{\sim} \begin{cases} AE' \frac{\alpha}{4} \cot(\pi\alpha)\hat{r}^{\alpha-1}, & \frac{1}{2} < \alpha < 1 \\ \frac{AE'}{4\pi} \ln \hat{r}, & \alpha = 1 \end{cases} \tag{13}$$

and $p = C$ for $\alpha = 1/2$. Assuming that $\hat{r} \ll R$ in (7), substituting the leading behaviours for the apertures (12) and pressures (13) into (7), and replacing each of the terms in the lubrication equation by their dominant asymptotic behaviour, we obtain

$$\dot{A}\hat{r}^{\alpha} + \alpha V A \hat{r}^{\alpha-1} - \alpha(\alpha-1)(\alpha-\frac{1}{2})\cot(\pi\alpha)\frac{A^4E'}{\mu'}\hat{r}^{4\alpha-3} + \hat{g} = 0 : \ \frac{1}{2} < \alpha < 1 \tag{14}$$

$$\dot{A}\hat{r} + VA - \frac{A^4E'}{2\mu'\pi}\hat{r} + \hat{g} = 0 : \ \alpha = 1 \tag{15}$$

For exponents in the range $\frac{1}{2} < \alpha \le 1$, vertex solutions are obtained by identifying the dominant balances between the different terms in (14) and (15).

After arrest $V \le 0$ and the leak-off term $\hat{g}$ is no longer singular and, as time progresses, approaches a value that is spatially uniform. Thus, in order to perform the local analysis to determine asymptotic solutions after arrest, $\hat{g}$ will, to first order, be assumed to be spatially homogeneous in the tip region and denoted by $\hat{g}_0(t)$.

3.1.1. Propagating hydraulic fracture ($K = K', V > 0$)

The vertex solutions for a propagating hydraulic fracture are well established (Detournay, 2016). The k'-asymptote $\hat{w}_{k'}$ associated with the fracture toughness is given by LEFM, which comes directly from the propagation condition (11); the $\tilde{m}$-asymptote $\hat{w}_{\tilde{m}}$ associated with leak-off is obtained by balancing the third and fourth terms in (14) with $\hat{g}$ approximated by $\hat{g} \sim C'\left(\frac{V}{\hat{r}}\right)^{1/2}$ close to the tip; the m-asymptote $\hat{w}_m$ associated with viscous dissipation is obtained by balancing the second and third terms in (14). These asymptotes are respectively given by

$$\hat{w}_{k'} = l_{k'}^{1/2}\hat{r}^{1/2}, \ \hat{w}_{\tilde{m}} = \beta_{\tilde{m}} l_{\tilde{m}}^{3/8}\hat{r}^{5/8}, \text{ and } \hat{w}_m = \beta_m l_m^{1/3}\hat{r}^{2/3} \tag{16}$$

where the following length scales have been defined: $l_{k'} = \left(\frac{K'}{E'}\right)^2$, $l_{\tilde{m}} = \left(\frac{4\mu' V C'^2}{E'}\right)^{1/3}$, and $l_m = \frac{\mu' V}{E'}$, and the constants are given by $\beta_{\tilde{m}} = 4/(15(\sqrt{2}-1))^{1/4} \approx 2.5336$ and $\beta_m = 2^{1/3}3^{5/6} \approx 3.1473$.

3.1.2. Arrest of a hydraulic fracture ($0 \le K < K', \ V = 0$)

The arrest asymptotes, recently described in Peirce and Detournay (2022a), are: the k-asymptote $\hat{w}_k$ determined from LEFM in terms of the stress intensity factor K, which decreases from K' to 0 as the fracture deflates as a result of fluid leaking from the fracture into the porous medium; and the ephemeral g-asymptote $\hat{w}_g$, associated with the arrest–recession transition, which is obtained by noting that $V = 0$ and matching the third and fourth terms in (14) with $\hat{g} \sim \hat{g}_0$. These asymptotes are respectively given by:

$$\hat{w}_k = l_k^{1/2}\hat{r}^{1/2} \text{ and } \hat{w}_g = \beta_g l_g^{1/4}\hat{r}^{3/4}, \tag{17}$$

where $l_k = \left(\frac{K}{E'}\right)^2 = \varepsilon_k^2 l_{k'}$ is the stress intensity length scale, ε_k is a dimensionless stress intensity parameter defined in terms of the stress intensity factor K as follows:

$$\varepsilon_k := \frac{K}{K'} = \frac{K_I}{K_{Ic}} < 1, \tag{18}$$

$l_g = \frac{\mu'\hat{g}_0}{E'}$ is the post-arrest leak-off length scale, and the constant $\beta_g = \left(\frac{64}{3}\right)^{1/4}$.

3.1.3. Recession asymptote - r-asymptote ($K = 0,\ V < 0$)

For $V < 0$, the g-asymptote with $\alpha = 3/4$ is inadmissible since the convective term $V\frac{\partial \hat{w}}{\partial \hat{r}}$, which is now present, violates the dominant balance that applied when the fracture was at rest. Thus the only admissible balance occurs if $\alpha = 1$, for which the leading order match between the second and fourth terms in (15) yields the r-asymptote:

$$\hat{w}_r = \frac{\hat{g}_0}{|V|}\hat{r} = \frac{l_g}{l_r}\hat{r} = \frac{\hat{r}}{\varepsilon_r} \tag{19}$$

where we have introduced the length scale $l_r = \frac{\mu' |V|}{E'}$ and the parameter $\varepsilon_r = \frac{|V|}{\hat{g}_0} = \frac{l_r}{l_g}$. There is also a match at the next order between the first and third terms in (15).

3.2. The connection problem to establish edge solutions

In the previous subsection we presented the multiple vertex asymptotes that apply for propagating HF, arrested HF, and receding HF — each corresponding to a different physical process that is assumed to be dominant at the tip. When multiple physical processes compete in the tip region then the asymptotic solution involves multiple vertex asymptotes. Since the solutions connecting the multiple vertex asymptotes that are present for propagating hydraulic fractures are already well established (Garagash et al., 2011; Dontsov and Peirce, 2015), in this section we will restrict ourselves to summarizing the recently developed 'edge' solutions (Peirce and Detournay, 2022a) that connect the two vertex solutions that are present during each of the arrest and recession phases of hydraulic fracture deflation.

3.2.1. Nonsingular Fredholm integral equation

By considering the limit as $\hat{r} \to 0$, (2) and (6) can be shown to reduce to those of a stationary semi-infinite fracture in a state of plane strain moving with a constant velocity V or deflating while arrested (Peirce and Detournay, 2008). For this problem the equation relating the pressure to the fracture aperture becomes:

$$\hat{p} = -\frac{E'}{4\pi}\int_0^\infty \frac{\partial \hat{w}}{\partial \hat{s}}\frac{\mathrm{d}\hat{s}}{\hat{s}-\hat{r}}, \tag{20}$$

Garagash and Detournay (2000) showed that, provided $\hat{p} \overset{\hat{r}\to\infty}{\sim} O(\hat{r}^{-\gamma})$ for $\gamma > 0$, the integral equation (20) can be inverted to yield an expression for $\hat{w}$ in terms of an integral operator acting on $\hat{p}$, which, upon integrating by parts (Dontsov and Peirce, 2015), yields the following integral expression for $\hat{w}(\hat{r})$

$$\hat{w}(\hat{r}) = \frac{K}{E'}\hat{r}^{1/2} - \frac{4}{\pi E'}\hat{r}^{1/2}\int_0^\infty \hat{s}^{1/2} G\left(\left(\frac{\hat{s}}{\hat{r}}\right)^{1/2}\right)\frac{d\hat{p}(\hat{s})}{d\hat{s}}d\hat{s} \tag{21}$$

where K is the scaled stress intensity factor and the kernel is given by $G(t) = \frac{1-t^2}{t}\ln\left|\frac{1+t}{1-t}\right| + 2$. The integral operator in (21) is non-singular since $0 < G(t) \le 4$.

Considering the lubrication equation (7) in the limit $\hat{r} \to 0$, discarding the term $\frac{\partial \hat{w}}{\partial t}$ since $\frac{\partial \hat{w}}{\partial t} \ll V\frac{\partial \hat{w}}{\partial \hat{r}}$ for $\frac{1}{2} \le \alpha \le 1$, integrating, and rearranging, we obtain the following equation for the pressure gradient:

$$\frac{d\hat{p}}{d\hat{r}} = \frac{\mu'}{\hat{w}^2}\left(V + \frac{\hat{g}_0\hat{r}}{\hat{w}}\right) \tag{22}$$

Following (Dontsov and Peirce, 2015; Peirce and Detournay, 2022a) we use (22) to eliminate the pressure gradient from (21). We also define the scaled coordinate $\tilde{r} = \left(\frac{\hat{r}}{l_e}\right)^{1/\delta_1}$, where l_e is a suitably chosen edge length scale, and the scaled aperture $\tilde{w} = \frac{\hat{w}}{\hat{w}_a}$, where $\hat{w}_a$ is the vertex asymptote that occupies the tip region, to obtain the following nonlinear, non-singular, Fredholm integral equation of the second kind:

$$\tilde{w}(\tilde{r}) = \lambda + \frac{4\delta_1}{\pi}\tilde{r}^{\delta_2-1}\int_0^\infty G\left(\left(\frac{\tilde{s}}{\tilde{r}}\right)^{\delta_2}\right)\frac{\tilde{s}^{\delta_3}\,(1-\tilde{w}(\tilde{s}))^{\delta_4}}{\tilde{w}(\tilde{s})^3}d\tilde{s},\ \ \tilde{w}(0) = 1 \tag{23}$$

Here the parameters λ and δ_k change depending on whether the arrest or recession edge is being considered. Because (23) is nonsingular it can be reduced to a system of nonlinear equations for $\tilde{w}$ by discretization using standard quadratures.

3.2.2. Arrest edge — the $k-g$ edge solution

Since $\hat{r}^{1/2} \gg \hat{r}^{3/4}$ as $\hat{r} \to 0$, the k-asymptote will dominate the solution in the tip region and the g-asymptote will only manifest itself as we move farther from the tip. The extent of the region closest to the tip that is occupied by the k-asymptote decreases with K while the fracture is deflating while arrested. The g-asymptote expands into the tip region that has been vacated by the k-asymptote until $K = 0$, at which instant the g-asymptote occupies the tip region completely. We therefore seek the $k-g$ edge solution $\tilde{w}_{kg}$ that connects the inner solution $\hat{w} \overset{\hat{r}\to 0}{\to} \hat{w}_k$ to the outer solution $\hat{w} \overset{\hat{r}\to\infty}{\to} \hat{w}_g$.

In this case we choose $l_e = l_{kg} = l_k^2/l_g$ and, because the k-asymptote occupies the tip region while $K > 0$, we choose $\hat{w}_a = \hat{w}_k$. For this edge solution $\tilde{w} = \tilde{w}_{kg}$, and the appropriate parameters in the integral equation (23) are:

$$V = 0 : \lambda = 1,\ \delta_1 = 2,\ \delta_2 = 1,\ \delta_3 = 1,\ \delta_4 = 0 \tag{24}$$

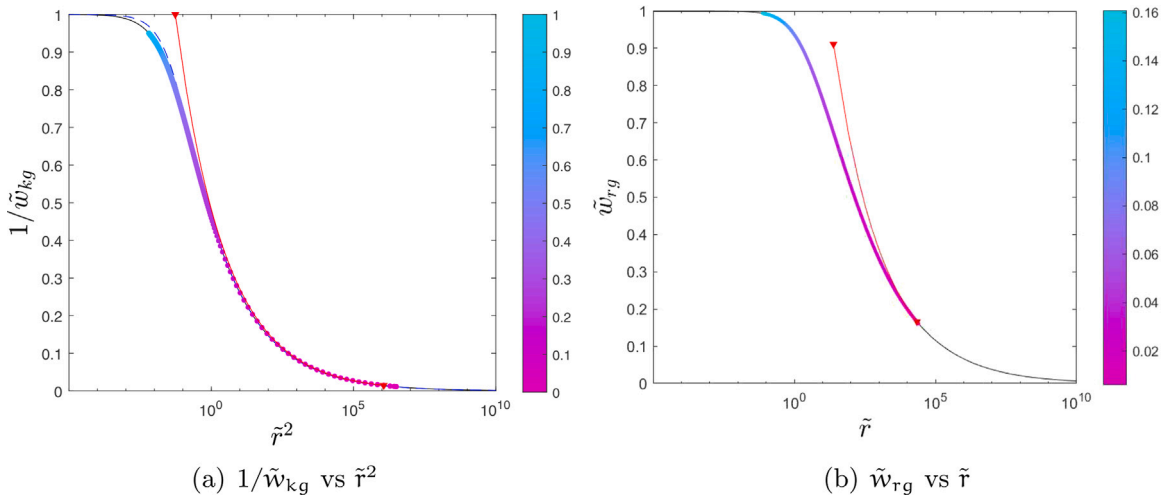

Fig. 2. (a) Plot of the reciprocal of the scaled aperture $1/\tilde{w}_{kg}$ as a function of $\tilde{r}^2$ for the $k-g$ edge asymptote. The solid black curve represents the numerical solution to (23) with the $k-g$ parameter set given in (24), while the dashed blue curve represents the approximate solution provided by (25). (b) Plot of the scaled aperture $\tilde{w}_{rg}$ as a function of $\tilde{r}$ for the $r-g$ edge asymptote. The solid black curve represents the numerical solution to (23) with the $r-g$ parameter set given in (26). For both (a) and (b), the red curves between the inverted red triangles represent the search path for a single time step followed by the fixed point scheme (29) for ε_k (a) and the fixed point scheme (30) for ε_r (b). The coloured dots represent the solutions for ε_k and ε_r for multiple time steps.

It is also possible (Dontsov and Peirce, 2015; Peirce and Detournay, 2022a) to obtain an approximate $k-g$ edge solution, which in this case has a relative error of less than 3%, by differentiating (23) and assuming a power law behaviour for $\tilde{w}_{kg}$ to obtain a separable ordinary differential equation, whose solution, along with the condition $\tilde{w}_{kg}(0)=1$, yields

$$\tilde{w}_{kg} \approx \left(1+\beta_g^4\tilde{r}^2\right)^{1/4} \quad \text{or} \quad \hat{w}_{kg} \approx l_k^{1/2}\hat{r}^{1/2}\left(1+\beta_g^4\frac{\hat{r}}{l_{kg}}\right)^{1/4} \tag{25}$$

In Fig. 2(a) we plot the reciprocal of the scaled aperture $1/\tilde{w}_{kg}$ as a function of $\tilde{r}^2=\hat{r}/l_{kg}$. We have chosen to plot the reciprocal of $1/\tilde{w}_{kg}$ as this emphasizes the variation in $\tilde{w}_{kg}$, with respect to the scaled variables, between the two asymptotic behaviours $\tilde{w}_{kg} \overset{\tilde{r}\to 0}{\to} \tilde{w}_k = 1$ representing the $\hat{w}_k$ asymptote and $\tilde{w}_{kg} \overset{\tilde{r}\to\infty}{\to} \tilde{w}_g = \beta_g\tilde{r}^{1/2}$ representing the $\hat{w}_g$ asymptote. The solid black curve in this figure represents the numerical solution to (23) with the $k-g$ parameter set given in (24). The dashed blue curve represents the approximate solution provided by (25).

3.2.3. Recession edge — the $r-g$ edge solution

Because $\hat{r}^{3/4} \gg \hat{r}$ as $\hat{r}\to 0$, we would expect the g-asymptote to dominate the r-asymptote closest to the tip. However, since the g-asymptote cannot exist at the tip for $V<0$, it is the r-asymptote that occupies the region closest to the tip while the g-asymptote will only manifest itself farther from the tip. Thus, as recession begins, i.e. $V<0$, the g-asymptote, which occupied the tip region completely at the instant $K=0$, is immediately displaced from the tip by the r-asymptote. We therefore seek the $r-g$ edge solution $\hat{w}_{rg}$ that connects the inner solution $\hat{w} \overset{\hat{r}\to 0}{\to} \hat{w}_r$ to the outer solution $\hat{w} \overset{\hat{r}\to\infty}{\to} \hat{w}_g$. In this case we choose $l_e = l_{rg} = l_r^4/l_g^3$ and, because the r-asymptote occupies the tip region from the instant the fracture starts to recede, we choose $\hat{w}_a = \hat{w}_r$. In this case the appropriate parameters in the integral equation (23) for $\tilde{w}=\tilde{w}_{rg}$ are:

$$V<0: \ \lambda=0, \ \delta_1=1, \ \delta_2=\frac{1}{2}, \ \delta_3=-\frac{3}{2}, \ \delta_4=1 \tag{26}$$

In Fig. 2(b), we plot $\tilde{w}_{rg}$ as a function of $\tilde{r}=\hat{r}/l_{rg}$. We observe that $\tilde{w}_{rg}$ approaches the limiting values $\tilde{w}_{rg} \overset{\tilde{r}\to 0}{\to} 1$ associated with $\hat{w}_r$ the r-vertex solution, and $\tilde{w}_{rg} \overset{\tilde{r}\to\infty}{\to} \tilde{w}_g = \beta_g\tilde{r}^{-1/4}$ associated with $\hat{w}_g$ the g-vertex solution, so that $0 \le \tilde{w}_{rg} = \frac{\hat{w}}{\hat{w}_r} \le 1$. The solid black curve in Fig. 2(b) represents the numerical solution to (23) with the $r-g$ parameter set given in (26).

3.3. Implementing the edge solutions

Multiscale tip asymptotic solutions have proven to be extremely useful in the development of numerical algorithms to model propagating fractures (Peirce and Detournay, 2008; Adachi and Detournay, 2008; Lecampion et al., 2013; Peirce, 2015, 2016; Dontsov and Peirce, 2017). These algorithms can achieve solutions with a high degree of precision, able to account for the multiscale behaviour at the finest length scale, while using a relatively coarse mesh. The fundamental idea (Peirce and Detournay, 2008; Peirce, 2015; Dontsov and Peirce, 2017) is to use a trial value of the fracture aperture $\hat{w}$, sampled at computational points within and adjacent to the fracture front, along with the applicable multiscale tip asymptote to estimate the fracture font location (or

equivalently the local front velocity) at the current step. The front position for propagating fractures is then adjusted iteratively and the aperture updated until both are consistent with the applicable multiscale asymptote.

In this subsection we describe how the $k-g$ edge solution can be used to determine accurate estimates of the stress intensity factor while the fracture is deflating during arrest as well as the time the fracture transitions from arrest to recession. We also describe how the $r-g$ edge solution can be used to determine accurate estimates of the negative velocity of the receding fracture front, which is particularly important shortly after the arrest–recession transition point. We will present the results of numerical simulations in which the solutions using the multiscale $k-g$ and $r-g$ asymptotes are compared to solutions that use the LEFM vertex asymptote to determine the stress intensity factor during arrest and only the linear r-asymptote to determine the negative velocity during recession.

In the results presented below we consider the implementation of the multiscale edge solutions and vertex solutions in an Implicit Moving Mesh Algorithm (IMMA) (Dontsov, 2016), which has been adapted to include the k-asymptote, the r-asymptote, as well as the multiscale $k-g$ and $r-g$ edge solutions.

3.3.1. Determining ε_k and ε_r using the multiscale asymptotes

Note that the $k-g$ edge solution $\tilde{w}_{kg}$ to (23) with the $k-g$ parameter set given in (24), shown in Fig. 2(a), and the $r-g$ edge solution $\tilde{w}_{rg}$ to (23) with the $r-g$ parameter set given in (26), shown in Fig. 2(b), are both universal in that they do not depend on any parameters. Indeed, the values of ε_k and ε_r are embedded in the scalings used to reduce these integral equations to a universal form so that they too are free of any parameters.

Determining ε_k and the stress intensity factor during arrest using $\tilde{w}_{kg}$:

Assuming that $\tilde{w}_{kg}(\tilde{r})$ is a known function of $\tilde{r}$, we can use the scaling defined for the $k-g$ edge solution to obtain

$$\hat{w} = \hat{w}_k(\hat{r})\tilde{w}_{kg}\left((\frac{\hat{r}}{l_{kg}})^{1/2}\right) = \varepsilon_k\hat{w}_{k'}(\hat{r})\tilde{w}_{kg}\left(\frac{1}{\varepsilon_k^2}(\frac{\hat{r}}{l_{k'g}})^{1/2}\right) \tag{27}$$

where $l_k = \varepsilon_k^2 l_{k'}$, $l_{kg} = \varepsilon_k^4 l_{k'g}$, and $l_{k'g} = \frac{l_{k'}^2}{l_g}$. Given trial values of $\hat{w}$, sampled at a certain distance $\hat{r}$ from the tip, (27) defines ε_k implicitly. From the behaviour $\tilde{w}_{kg} \overset{\tilde{r}\to 0}{\to} \tilde{w}_k = 1$, we observe that if the pair $(\hat{r},\hat{w})$ falls within the region under the k-umbrella, (27) reduces to the simple LEFM asymptote $\hat{w} = \varepsilon_k\hat{w}_{k'}(\hat{r})$ given in the first expression in (17), which is frequently used to determine the stress intensity factor. From the asymptotic behaviour $\tilde{w}_{kg} \overset{\tilde{r}\to\infty}{\to} \tilde{w}_g = \beta_g\tilde{r}^{1/2}$, we observe that if $\hat{r}$ is within the region under the umbrella of the g-asymptote, then upon simplification, ε_k vanishes from (27), which reduces to the g-asymptote $\hat{w}_g$ given in the second expression in (17). The implication of this latter reduction is that, once the solution is in the regime in which the g-vertex holds, it is not possible to obtain any information about ε_k and the stress intensity factor. It is interesting to note that if the second equation in (25) is used to determine ε_k, a real value of ε_k can only be determined provided $\hat{w} > \beta_g l_g^{1/4}\hat{r}^{3/4} = \hat{w}_g$.

Determining ε_r and the velocity during recession using $\tilde{w}_{rg}$:

Assuming that $\tilde{w}_{rg}(\tilde{r})$ is a known function of $\tilde{r}$, we can use the scaling defined for the $r-g$ edge solution to obtain

$$\hat{w} = \hat{w}_r(\hat{r})\tilde{w}_{rg}\left(\frac{\hat{r}}{l_{rg}}\right) = \frac{\hat{r}}{\varepsilon_r}\tilde{w}_{rg}\left(\frac{\hat{r}}{\varepsilon_r^4 l_g}\right) \tag{28}$$

where $l_r = \varepsilon_r l_g$ and $l_{rg} = \varepsilon_r^4 l_g$. Given trial values of $\hat{w}$, sampled a certain distance $\hat{r}$ from the tip, (28) defines ε_r implicitly. From the asymptotic behaviour $\tilde{w}_{rg} \overset{\tilde{r}\to 0}{\to} 1$, we observe that if the pair $(\hat{r},\hat{w})$ falls within the region under the r-umbrella, (28) reduces to the simple expression for ε_r in terms of the linear r-asymptote $\hat{w} = \hat{w}_r(\hat{r})$ given in (19). From the asymptotic behaviour $\tilde{w}_{rg} \overset{\tilde{r}\to\infty}{\to} \tilde{w}_g = \beta_g\tilde{r}^{-1/4}$, we observe that if $\hat{r}$ is within the region under the umbrella of the g-asymptote, then upon simplification ε_r vanishes from (28), which reduces to the g-asymptote $\hat{w}_g$ given in the second expression in (17). The implication of this latter reduction is that once the solution is in the regime in which the g-vertex holds, it is not possible to obtain any information about ε_r and the negative velocity of the receding fracture.

3.3.2. Fixed point schemes to determine ε_k and ε_r

Due to the loss of information by (27) and (28) when approaching the umbrella of the g-vertex $\hat{w}_g$, standard iteration schemes such as Newton's method applied to these two nonlinear equations do not provide stable algorithms to determine ε_k and ε_r, respectively. We observe that the general shape of the function $1/\tilde{w}_{kg}$ shown in (a) for the $k-g$ edge solution is very similar to that of the function $\tilde{w}_{rg}$ plotted in (b) for the $r-g$ edge solution. Both of these functions are bounded below by 0 and above by 1, which is a property we exploit below in developing stable fixed point iterative schemes.

A fixed point scheme to determine ε_k:

To establish a robust fixed point scheme to solve (27) for ε_k, we re-write this equation in the following recursive form:

$$\varepsilon_{k,i+1} = \frac{\hat{w}}{l_{k'}^{1/2}\hat{r}^{1/2}}\frac{1}{\tilde{w}_{kg}\left(\frac{1}{\varepsilon_{k,i}^2}(\frac{\hat{r}}{l_{k'g}})^{1/2}\right)} \tag{29}$$

Note that this recursion is expressed in terms of the function $1/\tilde{w}_{kg}$ plotted in Fig. 2(a). In this figure the red curve represents the trajectory of iterates $\varepsilon_{k,i}$ for a particular time step, which is selected, for illustrative purposes, to be later in the deflation process

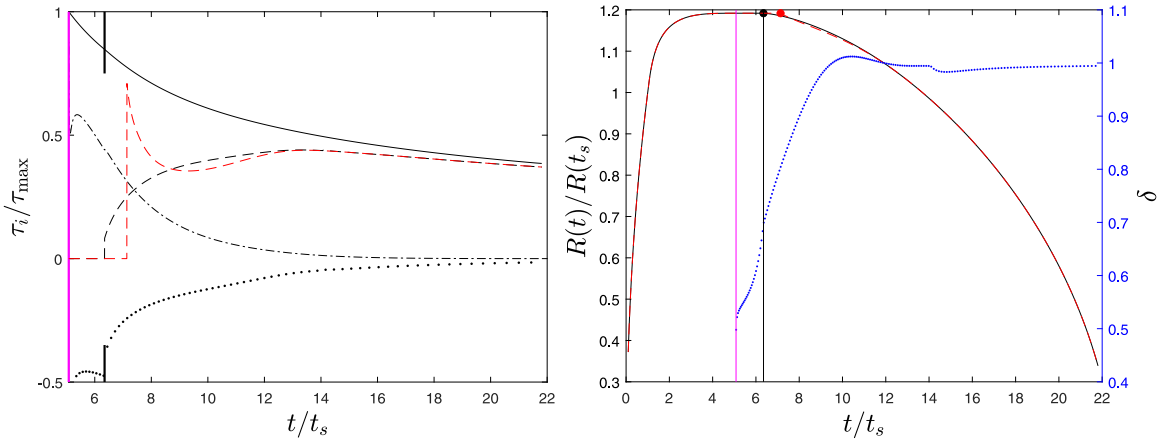

(a) Balance of terms (b) R/R$_s$ and δ vs t/t$_s$

Fig. 3. (a) Evolution of terms in the continuity equation from arrest to collapse $t \in (t_a, t_c)$ scaled to the maximum value on this interval: flux gradient $\frac{\partial}{\partial \hat{r}}\left(\frac{\hat{w}^3}{\mu'}\frac{\partial \hat{p}}{\partial \hat{r}}\right)$ (−·), $\frac{\partial \hat{w}}{\partial t}$ (···), $|V|\frac{\partial \hat{w}}{\partial \hat{r}}$ (−−), and $\hat{g}_0$ (solid). The black curves are extracted from an IMMA simulation that uses the multiscale $k-g$ and $r-g$ asymptotes, while the dashed red curve represents the convection term $|V|\frac{\partial \hat{w}}{\partial \hat{r}}$ when the simple LEFM k-asymptote is used to determine the stress intensity factor during arrest and only the linear r-asymptote is used to determine the negative velocity during recession. (b) The fracture radius scaled to the radius at shut-in $R/R(t_s)$ is plotted against the scaled time t/t_s for two different IMMA simulations, one using the multiscale $k-g$ and $r-g$ asymptotes (solid black) and the other (dashed red) using the simple LEFM k-asymptote estimate for the stress intensity factor during arrest and the linear r-asymptote to determine the negative velocity during recession. The blue dots represent estimates of the power law behaviour of $\hat{w}$ in the tip region from the formula $\delta = \frac{\hat{r}\frac{\partial \hat{w}}{\partial \hat{r}}}{\hat{w}}$.

because it is associated with a small value of ε_k. The sequence of iterates starts with the initial guess $\varepsilon_{k,0} = \frac{\hat{w}}{l_{k'}^{1/2}\hat{r}^{1/2}}$, which is obtained from the k-asymptote given in the first expression in (17), and indicated in Fig. 2(a) by the inverted red triangle for which $1/\tilde{w}_{kg} \sim 1$. These iterations terminate when the relative difference between successive iterates is less than 10^{-3} at the point indicated by the inverted red triangle on the lower part of the red curve. The coloured circles moving down the $1/\tilde{w}_{kg}$ curve in (a) represent the sequence of decreasing ε_k values (with values depicted on the colour bar) corresponding to decaying K values over multiple time steps as the fracture deflates while arrested.

A fixed point scheme to determine ε_r:

To establish a robust fixed point scheme to determine ε_r, we re-write (28) in the following recursive form in terms of the function $\tilde{w}_{rg}$ plotted in Fig. 2(b):

$$\varepsilon_{r,i+1} = \frac{\hat{r}}{\hat{w}}\tilde{w}_{rg}\left(\frac{\hat{r}}{\varepsilon_{r,i}^4 l_g}\right) \tag{30}$$

As with the ε_k case, the red curve in Fig. 2(b) represents the trajectory of iterates $\varepsilon_{r,i}$ for a single time step, while the coloured circles moving up the $\tilde{w}_{rg}$ curve represent the sequence of increasing ε_r values (with values depicted on the colour bar) corresponding to increasing $|V|$ values over multiple time steps as the receding fracture accelerates from the point of arrest.

3.3.3. The arrest–recession transition and the emergence of a dominant balance

Magnitude of terms in the lubrication equation:

In Fig. 3(a) we compare the relative magnitudes of each of the terms in the continuity equation (7) as a function of t/t_s from the time of arrest t_a to the time of collapse t_c. To establish the relative magnitudes, each of the terms τ_i in the continuity equation is divided by the maximum value $\tau_{\max} = \max_{t\in(t_a,t_c)}\max_i |\tau_i(t)|$ over the interval. The arrest time t_a is indicated in this plot by the vertical magenta line, while the arrest–recession transition point t_r is indicated by the thick black vertical lines that have been separated in order that the results of the plot are not obscured.

Comparison between IMMA solutions using edge asymptotes vs. vertex asymptotes:

The black curves in Fig. 3(a) represent the IMMA results obtained when the multiscale $k-g$ edge solution has been used to determine ε_k (and hence the stress intensity factor for the arrested deflating fracture) and the arrest–recession transition point t_r; and the $r-g$ edge solution has been used to determine ε_r and the magnitude of the receding fracture velocity. We will refer to this combined solution as *the multiscale edge* solution. The dashed red curve represents the IMMA result for the convective term $|V|\frac{\partial \hat{w}}{\partial \hat{r}}$ obtained when the simple LEFM asymptote given in the first expression in (17) is used to determine ε_k and the arrest–recession transition point t_r, while the linear r-asymptote is used to determine ε_r. We will refer to this combined solution as *the vertex* solution. We have chosen to restrict the comparison between these two different IMMA solutions to the convective term since

this term exhibits the largest difference between the two solutions and to keep the plot uncluttered. The solution (black −−) that uses multiscale edge asymptotes through the transition point t_r is much smoother than the corresponding vertex solution (red −−). Indeed, the vertex solution has a delayed transition point that exhibits an extreme jump discontinuity and a subsequent sharp drop to compensate until the transient effect of neglecting this multiscale behaviour decays around $t/t_s \sim 12$. The reason that using the r-vertex solution (19) over-estimates ε_r, and therefore the recession speed, is that it immediately attributes *all* the fracture aperture in the tip region to the linear asymptote. However, we know that, at the transition point t_r, the tip is fully occupied by the stationary g-asymptote. Therefore, it takes some time for the linear r-asymptote to displace this g-asymptote and occupy the tip at the length scale of one computational cell. Thus using the r-asymptote immediately, upon the initiation of recession, without waiting for the linear asymptote to occupy the tip element, is the cause of the observed jump in convective term. By contrast, the multiscale edge solution is able to allocate the appropriate contribution from the g-vertex to the tip apertures while the arrested fracture is deflating and, upon the initiation of recession, it is able to distribute the tip aperture correctly between the stationary g-vertex and the moving r-vertex and thereby identify the correct recession velocity.

Exponent evolution:

As a measure of the exponent of the average power law active in the tip region for the multiscale edge solution, we calculate the quotient $\delta = \frac{\hat{r}\frac{\partial \hat{w}}{\partial \hat{r}}}{\hat{w}}$ in the tip element, which, for a power law, would yield the value of the exponent. The derivative in this quotient is approximated by the second order backward difference approximation involving the three elements closest to the tip. The evolution of δ over the interval $t \in (t_a, t_c)$ is represented by the blue dots referenced to the right vertical axis in Fig. 3(b). As in (a) the arrest time t_a horizon is indicated in this plot by the vertical magenta line, while the arrest–recession transition t_r horizon is indicated by the vertical black line. We observe that δ evolves from the LEFM exponent of $1/2$ at the beginning of the arrest period, then passes through the g-vertex exponent $3/4$ close to the arrest–recession transition point t_r, and finally asymptotes to the r-vertex exponent 1 for $t/t_s \gtrsim 12$.

The emergence of a dominant balance:

It should be noted that the power laws in the range $\frac{1}{2} \le \alpha < 1$ encountered in propagating and arrested HF are singular and the vertex solutions associated with the smallest α are more dominant than the other vertex solutions that are present and therefore occupy the region closest to the tip. However, the r-asymptote is not singular, thus, immediately after the initiation of recession, the r-asymptote only applies very close to the tip and it takes a while for the leading order dominant balance to manifest itself any significant distance from the tip. Thus it takes a while for the linear r-asymptote to displace the g-asymptote that completely occupied the tip region at the instant of transition from arrest to recession. We observe from Fig. 3(a) that during the arrest period and at the start of the period of recession, the tip is governed by multiscale tip asymptotics so there is no dominant balance, which would typically be associated with a vertex solution. However, beyond $t/t_s \sim 12$, the leading order match starts to emerge between the second term $|V|\frac{\partial \hat{w}}{\partial \hat{r}}$ and the fourth term $\hat{g}$ in the lubrication equation (7). These were precisely the terms used in the dominant balance argument used to establish the r-vertex solution (19). We also note that the two terms $\frac{\partial \hat{w}}{\partial t}$ and $\frac{\partial}{\partial \hat{r}}\left(\frac{\hat{w}^3}{\mu'}\frac{\partial \hat{p}}{\partial \hat{r}}\right)$, which were found to match at the next order, can also be seen to asymptote to values of a comparable magnitude to one another, but which are much smaller than those of the dominant match.

Impact of using vertex asymptotes rather than edge asymptotes:

From Fig. 3(a) and the discussion above we see that using the vertex asymptotes to track the deflation of the hydraulic fracture results in the jump discontinuity in the convective term as one passes through the arrest–recession transition t_r. Although the existence of the g-vertex is ephemeral, we see that it is necessary to account for this special solution in both the multiscale $k-g$ and $r-g$ edge solutions in order to obtain a solution that will pass smoothly through the arrest–recession transition t_r. However, from Fig. 3(a) we observe that, if we use only the vertex asymptotes, the transients that result from the jump discontinuity decay fairly rapidly and the solution reverts to the same smooth solution produced by the multiscale edge asymptotes. Rather than only using individual terms in the lubrication equation to assess the impact of implementing simple vertex asymptotes as opposed to multiscale edge asymptotes on the quality of the solution, we also consider a more global quantity such as the fracture radius. In Fig. 3(b) we compare the scaled fracture radius $R(t)/R(t_s)$ as a function of t/t_s for the multiscale algorithm (solid black) to that for the simple vertex algorithm (dashed red). The recession initiation time t_r for the multiscale solution is denoted by the black circle and that for the simple vertex asymptotes is denoted by the red circle. The vertex solution only has a slightly delayed recession initiation time and exhibits only a slight deviation from the multiscale edge solution, which starts immediately after the onset of recession and persists until the transients decay. Indeed, these two solutions differ by less than $\frac{1}{2}\%$ throughout the duration of the simulation and are virtually indistinguishable in Fig. 3(b).

The analysis presented here has been important in order to provide a rigorous multiscale solution for the deflation of a radial hydraulic fracture during arrest and recession and particularly around the arrest–recession transition point t_r. However, this analysis also establishes that, unless the purpose of the modelling is to provide a smooth solution with great detail around the arrest–recession transition point t_r, a pragmatic, and much more efficient approach, would be to use a simpler algorithm based solely on vertex asymptotes.

4. Scaling analysis

4.1. Scaling

4.1.1. Scaling for a radial fracture subject to a constant injection rate Q_0

Following Detournay (2004, 2016), we introduce into the governing equations (2), (6), and (11) a length scale R_*, time scale t_*, characteristic aperture w_*, and pressure p_* such that $r = R_*\rho$, $t = t_*\tau$, $w = w_*\Omega$, and $p = p_*\Pi$. This makes it possible to identify the following five dimensionless groups:

$$\mathcal{G}_v = \frac{R_*^2 w_*}{Q_0 t_*},\ \mathcal{G}_m = \frac{\mu' Q_0}{w_*^3 p_*},\ \mathcal{G}_c = \frac{C' R_*^2}{t_*^{1/2} Q_0},\ \mathcal{G}_e = \frac{E' w_*}{R_* p_*},\ \text{and}\ \mathcal{G}_k = \frac{K' R_*^{1/2}}{E' w_*} \tag{31}$$

The storage–viscosity m-scaling can be identified by requiring $\mathcal{G}_v = \mathcal{G}_m = \mathcal{G}_e = 1$, from which it follows that the length R_m, aperture w_m, and pressure p_m scales are respectively given by

$$R_m = \left(\frac{E' Q_0^3 t^4}{\mu'}\right)^{1/9},\ w_m = \left(\frac{\mu'^2 Q_0^3 t}{E'^2}\right)^{1/9},\ \text{and}\ p_m = \left(\frac{\mu' E'^2}{t}\right)^{1/3} \tag{32}$$

while the dimensionless toughness and leak-off coefficient become

$$\mathcal{G}_k := \mathcal{K}_m = \left(\frac{K'^{18} t^2}{E'^{13} \mu'^5 Q_0^3}\right)^{1/18},\ \text{and}\ \mathcal{G}_c := \mathcal{C}_m(t) = \left(\frac{C'^{18} E'^4 t^7}{\mu'^4 Q_0^6}\right)^{1/18} \tag{33}$$

The leak-off–viscosity ($\tilde{m}$-scaling) can be obtained by requiring $\mathcal{G}_c = 1$ instead of $\mathcal{G}_v$ and the toughness (k -scaling) can be obtained by requiring $\mathcal{G}_k = 1$ instead of $\mathcal{G}_m$. We observe from (33) that the dimensionless toughness and leak-off coefficient for a radial fracture driven by a constant injection rate Q_0 both increase with time. We also observe that the transition time t_{mk} from viscosity to toughness dominated propagation and the transition time $t_{m\tilde{m}}$ from viscosity–storage dominated propagation to leak-off dominated propagation are given by

$$t_{mk} = \left(\frac{E'^{13} \mu'^5 Q_0^3}{K'^{18}}\right)^{1/2},\ t_{m\tilde{m}} = \left(\frac{\mu'^4 Q_0^6}{C'^{18} E'^4}\right)^{1/7} \tag{34}$$

while the propagation regime parameter ϕ is defined to be:

$$\phi = \frac{E'^{11} \mu'^3 Q_0 C'^4}{K'^{14}} = \left(\frac{t_{mk}}{t_{m\tilde{m}}}\right)^{\frac{14}{9}} \tag{35}$$

4.1.2. Scaling for a radial fracture after shut-in

In practice the evolution of a hydraulic fracture involves propagation due to the injection of a fluid at a flux Q_0 (considered here to be constant) followed by shut-in at a certain time t_s, after which the fracture may continue to propagate depending on the regime of propagation after shut-in. A propagating fracture in a permeable medium after shut-in will ultimately come to rest either due to excessive leak-off or because the stress intensity factor has dropped below the critical fracture toughness. In the latter case, there is an arrest period during which K decreases as the fracture continues to lose volume so that $\dot{w} < 0$, until $K = 0$ at which point transition to the recession asymptote is initiated and the fracture starts to recede.

The appropriate scaling for the dynamics of a hydraulic fracture with a fixed injected volume V_0 can be obtained (Mori and Lecampion, 2021) directly from those of a fracture driven by a constant flux Q_0 given in (32)–(33) by making the simple substitution $Q_0 = V_0/t$. In this case the length $R_m^V(t)$ and aperture $w_m^V(t)$ scaling factors are given by

$$R_m^V(t) = \left(\frac{E' V_0^3 t}{\mu'}\right)^{1/9} \text{and}\ w_m^V(t) = \left(\frac{\mu'^2 V_0^3}{E'^2 t^2}\right)^{1/9} \tag{36}$$

while the dimensionless toughness $\mathcal{K}_m^V(t)$ and leak-off $\mathcal{C}_m^V(t)$ parameters become

$$\mathcal{K}_m^V(t) = \left(\frac{K'^{18} t^5}{\mu'^5 E'^{13} V_0^3}\right)^{1/18} \text{and}\ \mathcal{C}_m^V(t) = \left(\frac{C'^{18} E'^4 t^{13}}{\mu'^4 V_0^6}\right)^{1/18} \tag{37}$$

Here we have followed (Mori and Lecampion, 2021) and used the superscript V to denote the scaling for a fracture with a fixed injected volume V_0 at time t. We observe from (37) that for a radial fracture with a fixed injected volume V_0, the viscous to toughness transition time t_{mk}^V and viscosity-storage to leak-off transition time $t_{m\tilde{m}}^V$ are respectively given by

$$t_{mk}^V = \left(\frac{\mu'^5 E'^{13} V_0^3}{K'^{18}}\right)^{1/5} \text{and}\ t_{m\tilde{m}}^V = \left(\frac{\mu'^4 V_0^6}{C'^{18} E'^4}\right)^{1/13} \tag{38}$$

Once shut-in has occurred these two transition times identify two different ways the fracture behaves after the time of arrest t_a, which, if $K' > 0$, is characterized by the stress intensity factor dropping below the critical fracture toughness and, as a result,

the velocity of the fracture going to zero. If $t_a \sim t^V_{mk} \ll t^V_{m\tilde{m}}$, then, at the time of arrest, the fracture is propagating in the toughness regime and still has a significant amount of fluid that needs to leak-off before recession can start. Conversely, if $t_a \sim t^V_{m\tilde{m}} \ll t^V_{mk}$, then, at the time of arrest, the fracture is already propagating in the leak-off regime and has lost sufficient fluid to preclude significant further propagation of the fracture. In this case recession starts almost immediately. In order to characterize these two arrest modes, we define the following arrest regime parameter ϕ^V for a radial hydraulic fracture with a fixed injected volume

$$\phi^V = \frac{t^V_{mk}}{t^V_{m\tilde{m}}} = \left(\frac{E'^{21} \mu'^5 C'^{10} V_0}{K'^{26}} \right)^{\frac{9}{65}} \tag{39}$$

If $\phi^V \gg 1$ then the transition to leak-off dominated propagation will occur significantly before there would be transition to toughness dominated propagation, so recession can be expected to start almost immediately and there will be a short arrest period. Conversely, if $\phi^V \ll 1$ then the transition to toughness dominated propagation will occur while the fracture is in the storage regime significantly before there would be a transition to leak-off dominated propagation. Thus at the time of arrest there is still a significant volume of fluid contained in the fracture that needs to leak off before recession can begin. Thus, in this case, there will be a significant period during which the fracture deflates while it is in a state of arrest. We observe that the parameter ϕ^V defined in (39) has no meaning in the zero toughness case since $t^V_{mk} = \infty$.

4.2. Characteristic power laws for arrest and recession

In the analysis that follows we will consider a given shut-in time t_s, which we will define with respect to the constant injection rate storage–leak-off transition time $t_{m\tilde{m}}$ in terms of the parameter ω defined by

$$\omega = \frac{t_s}{t_{m\tilde{m}}} \tag{40}$$

At shut-in, the injected volume is $V_s = Q_0 t_s$, the dimensionless leak-off coefficient at shut-in is $\mathcal{C}_m(t_s) := \mathcal{C}_s = \omega^{7/18}$, while the dimensionless toughness at shut-in is: $\mathcal{K}_m(t_s) := \mathcal{K}_s = \phi^{-1/14}\omega^{1/9}$. The fixed injected volume transition times, at which $\mathcal{K}^V_m(t) = 1$ and $\mathcal{C}^V_m(t) = 1$, can be expressed in terms of $\mathcal{K}_s$ and $\mathcal{C}_s$ as follows:

$$t^V_{mk} := t_s \mathcal{K}_s^{-\frac{18}{5}} \text{ and } t^V_{m\tilde{m}} := t_s \mathcal{C}_s^{-\frac{18}{13}} \tag{41}$$

We note that these are the expressions for t^V_{mk} and $t^V_{m\tilde{m}}$ that were established by Mori and Lecampion (2021) in terms of $\mathcal{K}_s$ and $\mathcal{C}_s$ respectively. Since the current paper is focussed on the dynamics of radial hydraulic fractures that deflate due to fluid losses to the permeable solid, we choose an alternative parameterization in terms of the dimensionless shut-in time ω, which makes it possible to unify the power laws for the zero and finite toughness cases — as leak-off is common to both. Moreover, the fixed injected volume arrest regime parameter ϕ^V is more appropriate for characterizing the arrest of a deflating fracture, than the propagation regime parameter ϕ that was defined to identify the viscous–toughness–leak-off modes of a propagating hydraulic fracture.

Now making use of (34) and (38) the following relationship can be established between the fixed injected volume transition time $t^V_{m\tilde{m}}$ and the constant injection rate storage–leak-off transition time $t_{m\tilde{m}}$ in terms of the dimensionless shut-in parameter ω :

$$t^V_{m\tilde{m}} = t_{m\tilde{m}} \omega^{\frac{6}{13}} = t_s \omega^{-\frac{7}{13}} \tag{42}$$

where the second relationship in (42) comes directly from the definition of ω.

Modes of arrest and recession: Using (42) and (39) we are now able to characterize the way in which the arrest time t_a and recession time t_r are impacted by the relative magnitudes of ϕ^V and ω.

- If $\phi^V \ll 1$:
  - If $\omega \ll 1$, it follows from (42) and (39) that

    $$t_s \ \& \ t^V_{mk} \ll t^V_{m\tilde{m}} \ll t_{m\tilde{m}}$$

    then, after shut-in arrest will be determined by $t_a \sim t^V_{mk}$ and recession will be determined by $t_r \sim t^V_{m\tilde{m}}$.
  - If $\omega \gg 1$, it follows from (42) and (39) that

    $$t_{m\tilde{m}} \ \& \ t^V_{mk} \ll t^V_{m\tilde{m}} \ll t_s$$

    then, after shut-in arrest and recession will be determined by $t_a \sim t_r \sim t_s$.
- If $\phi^V \gg 1$:
  - If $\omega \ll 1$, it follows from (42) and (39) that

    $$t_s \ \ll t^V_{m\tilde{m}} \ll t_{m\tilde{m}} \ \& \ t^V_{mk}$$

    then, after shut-in arrest and recession will be determined by $t^V_{m\tilde{m}}$, i.e. $t_a \sim t_r \sim t^V_{m\tilde{m}}$.
  - If $\omega \gg 1$, it follows from (42) and (39) that

    $$t_{m\tilde{m}} \ \ll t^V_{m\tilde{m}} \ll t_s \ \& \ t^V_{mk}$$

    then, after shut-in arrest and recession will be determined by $t_a \sim t_r \sim t_s$.

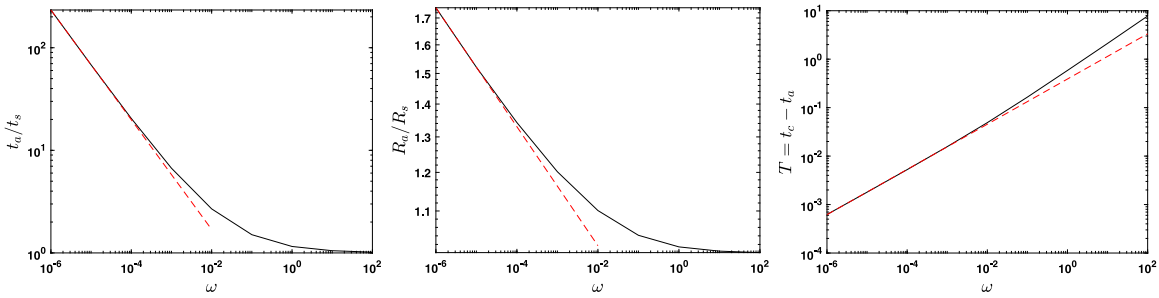

(a) t_a/t_s vs ω (b) R_a/R_s vs ω (c) $T/t_{m\tilde{m}}$ vs ω

Fig. 4. The solid black lines indicate the numerical solutions for the: (a) arrest time to shut-in time ratios, (b) arrest radius to shut-in radius ratios, and (c) deflation time to storage–leak-off transition time ratios $T/t_{m\tilde{m}}$ all plotted as a function of ω for the zero toughness case $K' = 0$. The dashed red lines represent log linear regressions for each of these plots using the first few data points.

4.2.1. Zero toughness case ($K' = 0$)

From (39) it follows that if $K' \to 0$ then $\phi^V \to \infty$, which, from the modes of arrest and recession identified above, clearly identifies the scaling for the time of arrest t_a, which, in this case, coincides with that of recession.

Arrest scaling: If the dimensionless shut-in time $\omega \ll 1$ then the arrest time t_a is determined by the time that the fixed injected volume fracture transitions from storage to leak-off dominated propagation, i.e.

$$t_a \sim t^V_{m\tilde{m}} = t_s \mathcal{C}_s^{-\frac{18}{13}} = t_s \omega^{-\frac{7}{13}} \tag{43}$$

The corresponding radius and aperture scales can be expressed in terms of ω, $R_s := R_m(t_s)$, and $w_s := w_m(t_s)$ as follows:

$$R_a := R^V_m(t_a) = \left(\frac{E' V_S^5}{\mu' C'^2}\right)^{\frac{1}{13}} = R_s \omega^{-\frac{7}{117}} \text{ and } w^V_m(t_a) = \left(\frac{\mu'^2 C'^4 V_S^3}{E'^2}\right)^{\frac{1}{13}} = w_s \omega^{\frac{14}{117}} \tag{44}$$

If $\omega \gg 1$, then shut-in occurs considerably later than the constant injection rate storage–leak-off transition time $t_{m\tilde{m}}$, so arrest can be expected to occur shortly after shut-in. These two limiting scalings can be summarized as follows:

$$t_a/t_s \sim \begin{cases} \omega^{-7/13} \text{ if } \omega \ll 1 \\ 1 \quad \text{if } \omega \gg 1 \end{cases} \tag{45}$$

$$R_a/R_s \sim \begin{cases} \omega^{-7/117} \text{ if } \omega \ll 1 \\ 1 \text{ if } \omega \gg 1 \end{cases} \tag{46}$$

$$w(t_a)/w_s \sim \begin{cases} \omega^{14/117} \text{ if } \omega \ll 1 \\ 1 \text{ if } \omega \gg 1 \end{cases} \tag{47}$$

In Fig. 4 the results of numerous numerical simulations using the IMMA algorithm described in Dontsov (2016), which has been adapted to include the arrest and recession asymptotes, are plotted for the zero toughness case. In 4(a) the ratios of the numerical arrest times t_a to the shut-in times t_s are plotted as a function of the dimensionless shut-in time ω. The red line represents a log linear regression of the ratio $t_a/t_s \sim A\omega^\alpha$ from the first few data points. The regression yields $\alpha = -0.535$, which is consistent with the power law given in (45). In 4(b), the ratios of the arrest radii R_a to the shut-in radii R_s are plotted as a function of the dimensionless shut-in time ω. The red line represents a log linear regression of the ratio $R_a/R_s \sim A\omega^\alpha$ from the first few data points. The regression yields $\alpha = -0.058$, which is consistent with the power law given in (46).

Deflation time scaling: We define the deflation time as $T = t_c - t_a$ and the reverse time variable to be $t' = t_c - t$, where t_a is the arrest time and t_c is the collapse time of the fracture. Motivated by the recession asymptote, in which the dominant balance is between the term representing the rate of change of aperture and the leak-off term, we consider the following model to estimate the deflation time T:

$$\frac{\partial w}{\partial t'} \sim \frac{C'}{\sqrt{T - t'}} \tag{48}$$

This model can also be interpreted as a dual reverse time problem in which the fracture is inflating from $w \approx 0$ at time $t' \approx 0$ and the aperture increases until time $t' = T$, at which time the leak-off term is singular. Integrating, it follows that $w \sim C'\sqrt{T}$, equating this aperture to $w^V_m(t_a)$, and using the fact that $w_s = C' t^{1/2}_{m\tilde{m}} \omega^{1/9}$, it follows that

$$T \sim t_{m\tilde{m}} \omega^{\frac{6}{13}} \tag{49}$$

In Fig. 4(c) the ratios of the deflation times to the storage–leak-off transition times $T/t_{m\tilde{m}}$ are plotted as a function of the dimensionless shut-in time ω. The dashed red line represents a log linear regression of $T/t_{m\tilde{m}} \sim A\omega^\alpha$ in which $\alpha = 0.467$, which is very close to the power law (49) predicted by the scaling analysis.

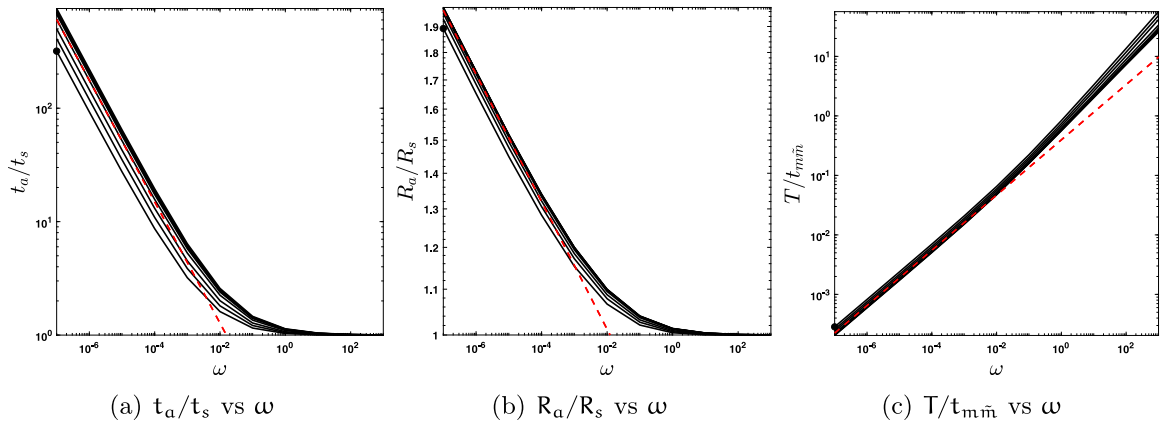

Fig. 5. The solid black lines indicate the numerical solutions for: (a) the arrest time to shut-in time ratios, (b) the arrest radius to shut-in radius ratios, and (c) the deflation time to storage–leak-off transition time ratios $T/t_{m\tilde{m}}$ all plotted as functions of ω for the range of values of the regime parameter $\phi^V \in \{0.05, 0.1, 0.2, 0.5, 1, 1.25, 1.5, 2, 3\}$. The dashed red lines represent log linear regressions for each of these plots using the first few data points for the case $\phi^V = 1$. The symbol • at the value $\omega = 10^{-7}$ is used to indicate curves corresponding to the smallest regime parameter $\phi^V = 0.05$. As ϕ^V increases the curves move progressively away from those with the • symbol. The dashed red lines represent log linear regressions for each of these plots using the first few data points for the case $\phi^V = 1$.

4.2.2. Finite toughness case ($K' > 0$)

Arrest scalings: If the dimensionless shut-in time $\omega \ll 1$, then the arrest time t_a is determined by when the fracture, which starts with a constant injected volume V_s at shut-in, transitions from viscosity to toughness dominated propagation, which, according to (39), occurs when

$$t_a \sim t^V_{mk} = \phi^V t^V_{m\tilde{m}} = t_s \phi^V \omega^{-\frac{7}{13}} \tag{50}$$

By comparing (50) and (45) we see the benefit of parameterizing the finite toughness case in terms of the *fixed injected volume* arrest regime parameter ϕ^V in that it results in the same power law dependence on ω. By contrast Mori and Lecampion (2021) chose a parameterization of the finite toughness case that used the propagation regime parameter ϕ defined in (35) as the ratio of the viscous-toughness to storage–leak-off transition times for a fracture driven to propagate by the injection of fluid volume at a *fixed rate* Q_0. Since this latter analysis was in terms of a parameter designed to characterize propagation under fixed rate injection, it is not suitable for the analysis of the arrest of fractures that propagate with a volume fixed at shut-in. Therefore the analysis (Mori and Lecampion, 2021) does not lead to power laws for the finite toughness case that also correlate with those for the zero toughness case.

As with the zero toughness case, the corresponding length and aperture scales can be obtained by substituting t_a into (36). If $\omega \gg 1$ then shut-in occurs considerably later than the constant injection rate storage–leak-off transition time $t_{m\tilde{m}}$, so arrest can be expected to occur shortly after shut-in. These two limiting scalings can be summarized as follows:

$$t_a/t_s \sim \begin{cases} \phi^V \omega^{-\frac{7}{13}} \text{ if } \omega \ll 1 \\ 1 \quad \text{if } \omega \gg 1 \end{cases} \tag{51}$$

$$R_a/R_s \sim \begin{cases} \left(\phi^V\right)^{\frac{1}{9}} \omega^{-\frac{7}{117}} \text{ if } \omega \ll 1 \\ 1 \text{ if } \omega \gg 1 \end{cases} \tag{52}$$

$$w_a/w_s \sim \begin{cases} \left(\phi^V\right)^{-\frac{2}{9}} \omega^{\frac{14}{117}} \text{ if } \omega \ll 1 \\ 1 \text{ if } \omega \gg 1 \end{cases} \tag{53}$$

By comparing (45)–(47) to (51)–(53) we observe that the parameterization of this scaling analysis by ω and ϕ^V leads to the same power law dependence of t_a/t_s, R_a/R_s and w_a/w_s on ω for the zero and finite toughness cases. The IMMA results for the finite toughness case are presented in Fig. 5. In Fig. 5(a) the ratios of the numerical arrest time t_a to the shut-in time t_s are plotted as a function of the dimensionless shut-in time ω for a range of values of the arrest regime parameter ϕ^V. The dashed red line represents a log linear regression of the ratio $t_a/t_s \sim A\omega^\alpha$ using the first few data points for the case $\phi^V = 1$, which yields $\alpha = -0.534$ - consistent with the power law given in (51). In Fig. 5(b) the ratios of the arrest radius R_a to shut-in radius R_s are plotted as a function of the dimensionless shut-in time ω for the same range of values of the regime parameter ϕ^V. The dashed red line represents a log linear

regression of the ratio $R_a/R_s \sim A\omega^{\alpha}$ using the first few data points for the case $\phi^V = 1$. The regression yields $\alpha = -0.057$, which is consistent with the power law given in (52). We observe that the t_a/t_s curves are further spread out than those of R_a/R_s because ϕ^V has a significantly larger range than $\left(\phi^V\right)^{\frac{1}{9}}$.

Deflation time scaling: In order to determine the deflation time T, as before we match $w \sim C'\sqrt{T}$ to the aperture given in (53) and use $w_s = C' t_{m\tilde{m}}^{1/2}\omega^{1/9}$ to obtain

$$T \sim t_{m\tilde{m}} \left(\phi^V\right)^{-\frac{4}{9}} \omega^{\frac{6}{13}} \tag{54}$$

Comparing (49) to (54) we observe that the parameterization ω and ϕ^V leads to the same power law dependence of T on ω for both the zero and finite toughness cases.

In Fig. 5(c) the ratio of the deflation time to the storage–leak-off transition time $T/t_{m\tilde{m}}$ is plotted as a function of the dimensionless shut-in time ω for the same range of ϕ^V values. The dashed red line represents a log linear regression of $T/t_{m\tilde{m}} \sim A\omega^{\alpha}$ using the first few data points for the case $\phi^V = 1$. The regression yields $\alpha = 0.462$, which is very close to the power law (54) predicted by the scaling analysis.

5. Deflating fracture solution

5.1. Solution landscape represented by the evolving fracture radius R

In Table 1 the ratio of the radius scaled to the shut-in radius $R(t)/R_s$ is plotted as a function of the scaled time t/t_s for $\phi^V = 0.1,\ 0.5,\ 1$ and $\omega = 10^{-6},\ 10^{-3}, 1, 10$. The value of ϕ^V is constant for each column of the table while the value of ω is constant for each row. The red parts of the curve represent the dynamics up to the shut-in time t_s, which is designated by a red asterisk $*$. The subsequent black part of the curve between the red shut-in point $*$ and the magenta arrest point $\bullet$, represents the radius between the time fluid injection ceased and the point of arrest. The magenta part of the curve between the arrest point $\bullet$ and the recession initiation point $\blacktriangledown$ represents the period during which the fracture continues to lose fluid while arrested, so that $V = 0$ and $\frac{\partial w}{\partial t} < 0$. The subsequent black part of the curve starting with $\blacktriangledown$ represents the decreasing fracture radius R while the fracture recedes. Scanning down the first column $\phi^V = 0.1$, we observe that the collapse time occurs a factor of 870 times later than the shut-in time for the case $\omega = 10^{-6}$, which is reduced to 22.8 for $\omega = 10^{-3}$, which decreases to 1.8 for $\omega = 1$, and is reduced further to 1.3 for the case $\omega = 10$. These factors remain almost constant for the other two columns. Scanning across the rows, the proportion of the time spent deflating while arrested (magenta portions of the curves) decreases as ϕ^V is increased, while the proportion of time spent on recession alone remains almost constant. This behaviour is to be expected given the definition of ϕ^V in (39). The data used to generate the plots in Table 1 and Fig. 6 are available for download (Peirce, 2022).

5.2. Aperture and pressure profiles

In Fig. 6 we provide more detailed plots of the numerical solutions for the first column in Table 1 associated with the value of the arrest regime parameter $\phi^V = 0.1$ and the values of the dimensionless shut-in time $\omega = 10^{-6},\ 10^{-3},\ 1,\ 10$ located in (a)–(d), respectively. In the first row for each parameter pair (ϕ^V, ω), we provide plots of the scaled radius $R(t)/R_s$, the efficiency $\eta(t)$, and the wellbore pressure $p(0,t)$ scaled to the wellbore pressure at shut-in, $p_s := p(0,t_s)$, against the scaled time t/t_s. The efficiency is defined to be the ratio of the volume of fluid in the fracture to the pumped volume $V_f(t)$ defined below (10)

$$\eta(t) := \frac{2\pi \int_0^R w(r,t) r dr}{V_f(t)},$$

In the second row of each of (a), (b), (c), and (d), we provide plots of the fracture aperture w scaled to the maximum aperture at shut-in, $w_s := w(0,t_s)$, against the scaled radius r/R_s for a number of sample times. The red curves represent the fracture aperture at shut-in $t = t_s$. Except for a small region near the tip, many of the red curves extend beyond the maximum ordinate range, which, for clarity, have been restricted to a maximum value set by the arrest aperture profile. The magenta curves represent the aperture profiles for the hydraulic fracture while it deflates during the arrest phase. The solid magenta curve, indicated by the magenta circle $\bullet$ at the wellbore, is the aperture profile sampled at the point of arrest $t = t_a$. The black curves correspond to the aperture profiles while the hydraulic fracture is receding. The curve indicated by the black circle $\bullet$ at the wellbore is the aperture profile sampled at the recession initiation time $t = t_r$. For the four cases considered in Fig. 6 the scaled sample times t/t_s that correspond to each of the symbols located at the wellbore are listed in Table 2. These symbols have also been indicated on the time evolution plots provided in the first rows of plots (a)–(d).

As the fracture approaches the collapse time t_c it can be seen that the solutions are approximately self-similar. Indeed, it is possible to derive the following sunset similarity solution (Peirce and Detournay, 2022b) for a receding radial fracture in a permeable elastic medium:

$$w(s,t) = g_0(t_c - t)\left[1 - \left(\frac{r}{R}\right)^2\right], \quad R = \Lambda(t_c - t)^{1/2} \tag{55}$$

where g_0 is the constant leak-off asymptote $g = \frac{C'}{\sqrt{t - t_o(r)}} \overset{t \to t_c}{\sim} g_0$ and Λ is determined by the amount of fluid in the fracture at a given radius R on the way to collapse. For the last three sample times, indicated by the ($\blacklozenge, \blacktriangle, \blacktriangleright$) symbols at the wellbore, the sunset

Table 1
Scaled radius R(t)/R$_s$ vs. t/t$_s$ plotted for different ϕ^V and ω values.

ω/ϕ^V	0.1	0.5	1
10^{-6}	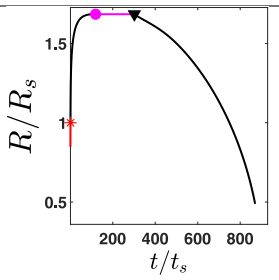	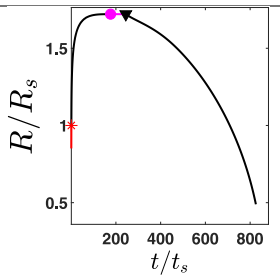	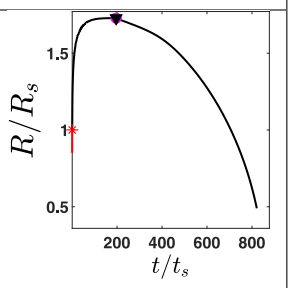
10^{-3}	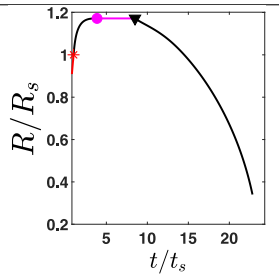	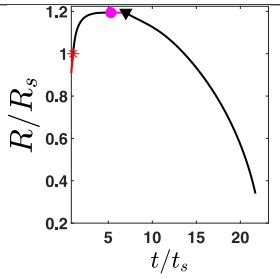	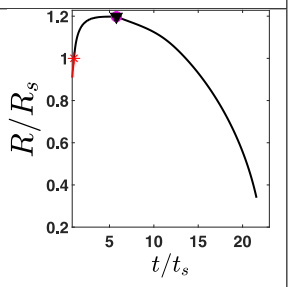
1	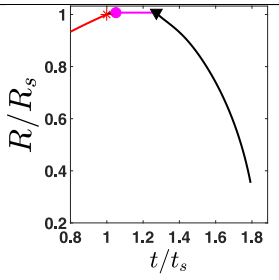	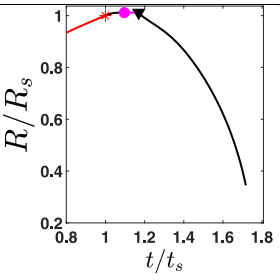	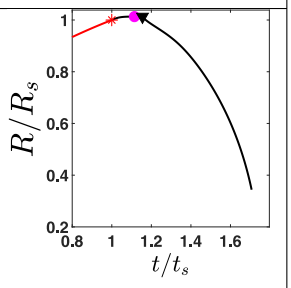
10	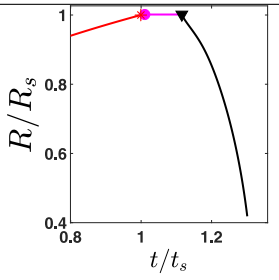	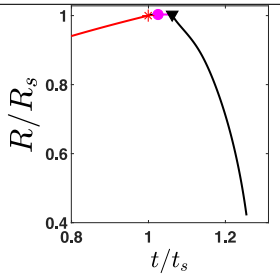	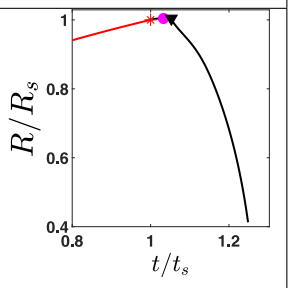

Table 2
The scaled sample times t/t$_s$ corresponding to each of the markers in Fig. 6.

Subfigure	ω	•	♦	▲	•	▼	♦	▲	▶
(a)	10^{-6}	119	165	256	302	472	655	770	844
(b)	10^{-3}	3.8	5.0	7.3	8.5	12.7	17.3	20.22	22.16
(c)	1	1.05	1.11	1.22	1.27	1.41	1.58	1.69	1.77
(d)	10	1.01	1.04	1.09	1.12	1.16	1.23	1.27	1.29

solution (55) is represented by the dashed blue curves for comparison with the numerical solution. As $t \to t_c$ these two solutions show close agreement.

In the third row of each of (a), (b), (c), and (d), we provide plots of the fracture pressure p scaled to the wellbore pressure at shut-in, p_s, against the scaled radius $r/R(t_s)$ for a number of sample times. The red curves represent the pressure profile at shut-in $t = t_s$. Except for a small region near the tip, many of the red curves extend beyond the maximum ordinate range, which, for clarity, have been restricted to a maximum value set by the arrest pressure profile. The magenta curves represent the pressure profiles for

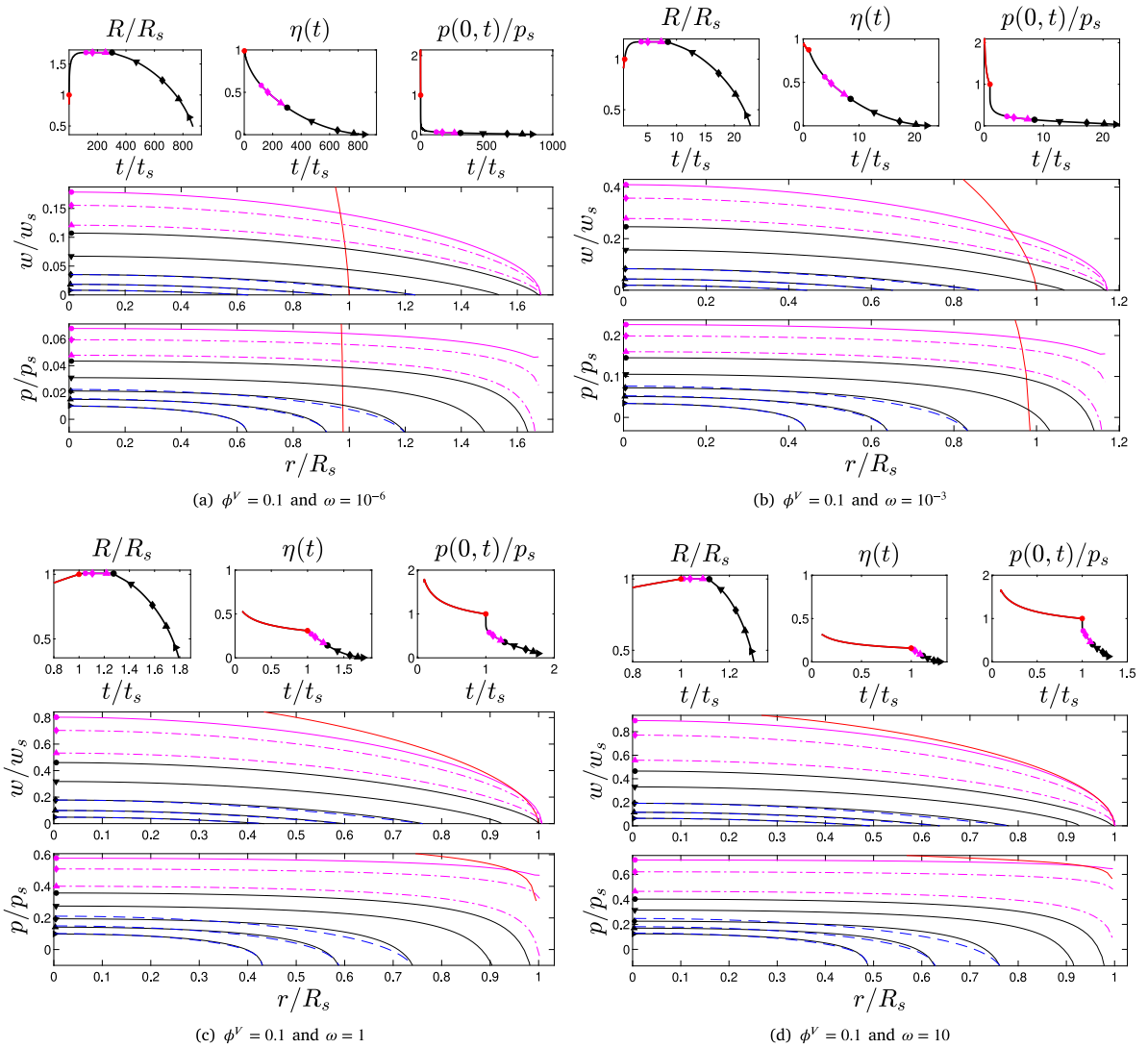

(a) $\phi^V = 0.1$ and $\omega = 10^{-6}$

(b) $\phi^V = 0.1$ and $\omega = 10^{-3}$

(c) $\phi^V = 0.1$ and $\omega = 1$

(d) $\phi^V = 0.1$ and $\omega = 10$

Fig. 6. For each of (a), (b), (c), and (d) the following plots are provided: Top row: scaled fracture radius $R(t)/R(t_s)$, fracture efficiency η, and wellbore pressure $p(0,t)$ scaled to the wellbore pressure p_s at shut-in all plotted as a function of t/t_s; Middle row: snapshots of the fracture aperture w after arrest scaled to the maimum aperture w_s at shut-in plotted as a function of $r/R(t_s)$; Bottom row: snapshots of the fracture pressure p after arrest scaled to the wellbore pressure p_s at shut-in plotted as a function of $r/R(t_s)$.

the hydraulic fracture while it deflates during the arrest phase. The solid magenta curve, indicated by the magenta circle • at the wellbore, is the pressure profile sampled at the point of arrest $t = t_a$. The black curves correspond to the pressure profiles while the hydraulic fracture is receding. The curve indicated by the black circle • at the wellbore is the pressure profile sampled at the recession initiation time $t = t_r$. As with the aperture profiles, the scaled sample times t/t_s that correspond to each of the symbols located at the wellbore are listed in Table 2. The pressure field associated with the sunset solution can be obtained by substituting (55) into (2) and evaluating the resulting integral numerically. For the last three sample times indicated by the (◆, ▲, ▶) symbols at the wellbore, the sunset pressure profile is represented by the dashed blue curves for comparison with the numerical solution. As $t \to t_c$ these two solutions show close agreement.

5.3. Solution using field parameters

We have demonstrated that the dimensionless shut-in time ω and regime parameter ϕ^V fully characterize the arrest and recession dynamics of deflating radial hydraulic fractures. In order to get an idea of the range of values that the dimensionless pair (ω, ϕ^V) might assume when typical field parameters are used, consider the following ranges of material parameters: $E' \sim 1 - 30$ GPa, $\mu' \sim 10^{-2}$–10 Pa s, $C' \sim 10^{-5}$–10^{-8} m s$^{-1/2}$, $K' \sim 0.3$–3 MPa m$^{1/2}$, $t_s \sim 3600$ s and $Q_0 \sim 10^{-3}$–10^{-1} m^3 s^{-1}. For these ranges of material and injection parameters, the range in the values assumed by the dimensionless parameters is $10^{-10} \lesssim \omega \lesssim 3$ and $10^{-10} \lesssim \phi^V \lesssim 10^4$.

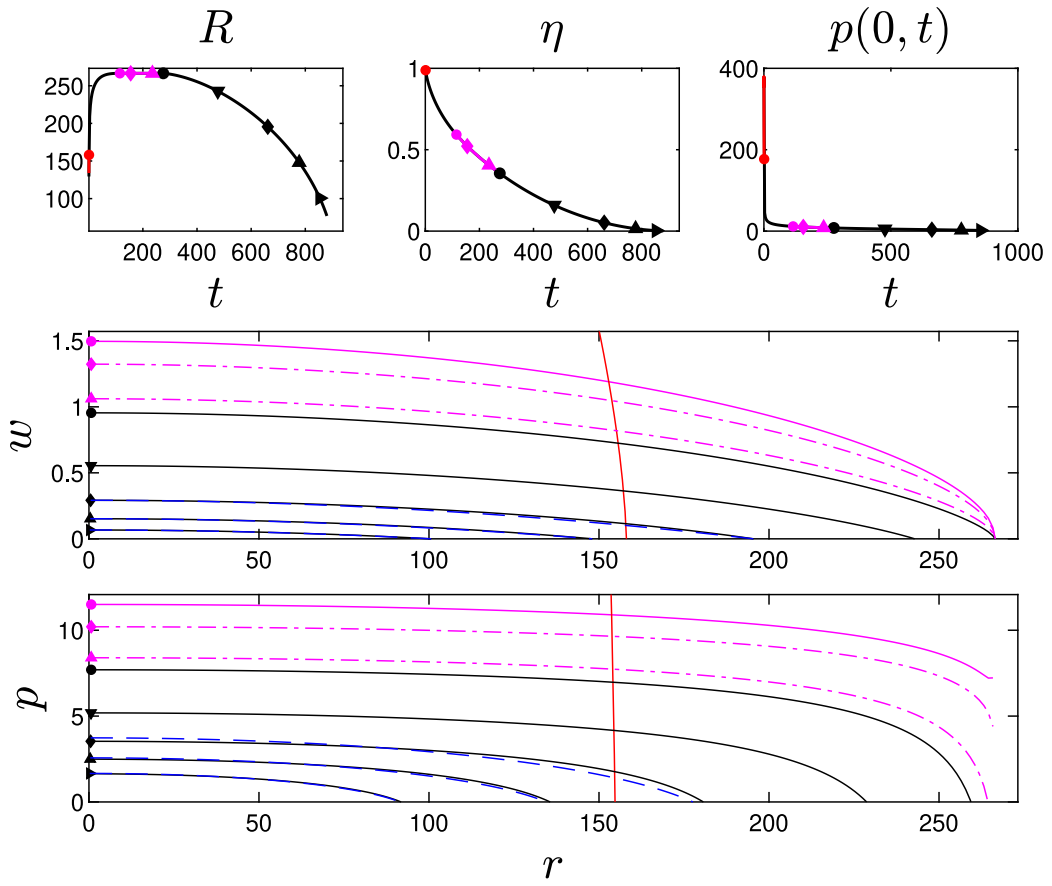

Fig. 7. Top row: fracture radius $R(t)$ [m], fracture efficiency η, and wellbore pressure $p(0,t)$ [kPa] all plotted as a function of t measured in hours [h]; Middle row: snapshots of the fracture aperture w [mm] after arrest plotted as a function of r [m]; Bottom row: snapshots of the pressure p [kPa] after arrest plotted as a function of r [m].

We now provide a solution in physical units for a deflating radial hydraulic fracture that arrests and recedes for input parameters that are within the range one might expect in the field. Let $E' = 5$ GPa, $\mu' = 0.5$ Pa s, $C' = 0.535 \times 10^{-6}$ m s$^{-1/2}$, $K' = 0.5493114$ MPa m$^{1/2}$, $t_s = 3600$ s and $Q_0 = 10^{-1}$ m^3 s^{-1}. This parameter set has been chosen so that the dimensionless shut-in time $\omega \sim 10^{-6}$ and regime parameter $\phi^V \sim 0.1$, which correspond to the case considered in Fig. 6(a) in which the results were given in scaled form. The resemblance between the results in Figs. 7 and 6(a) is clear. For the time evolution plots shown in the first row of Fig. 7 the resemblance is emphasized by the fact that t is plotted in hours while the shut-in time $t_s = 3600$ s or 1 h. Indeed, the plots are almost identical, except that the scales on the axes are now provided in physical units rather than scaled form. The same symbol and line conventions have been used for Fig. 7 as those defined for Fig. 6.

6. Conclusions

In this paper we have considered the post shut-in dynamics of a radial hydraulic fracture in a porous elastic medium. We have shown how recently developed multiscale tip asymptotic solutions for hydraulic fractures during arrest and recession, can be implemented in a numerical scheme that is able to capture the arrest–recession transition while using a relatively coarse mesh. This algorithm uses the arrest multiscale tip asymptote $\hat{w}_{kg}$ to determine the decreasing stress intensity factor K as the fracture deflates and the ephemeral g-asymptote displaces the k-asymptote at the fracture tip. At the transition point, characterized by $K = 0$, the g-asymptote occupies the tip region completely. The algorithm then uses the recession multiscale tip asymptote $\hat{w}_{rg}$ to determine the receding tip speed $|V|$ as the g-asymptote is gradually displaced by the linear r-asymptote. By using the arrest and recession multiscale asymptotes the algorithm is able to capture the arrest–recession transition smoothly. The solution that uses the two multiscale asymptotes $\hat{w}_{kg}$ and $\hat{w}_{rg}$ to effect the arrest–recession transition is compared to a solution that uses only the k and r-vertex solutions. The solution that uses only vertex asymptotes exhibits jump discontinuities through the arrest–recession transition point, while the multiscale solution is smooth. This is because, immediately after recession starts, the linear r-asymptote is only valid on a much smaller length scale compared to that of a tip element. Thus ascribing all the aperture in the tip to the r-asymptote and ignoring the contribution of the g-asymptote, results in a recession velocity that is much too large. However, using the

multiscale asymptotes, one is able to apportion these components correctly and in an adaptive fashion to achieve a smooth solution. We demonstrate that even while using a coarse mesh the multiscale asymptotes are able to capture the power law exponents in the range $1/2 \leq \delta \leq 1$, which are predicted by asymptotic analysis. Despite the jump discontinuity through the arrest–recession transition exhibited by the algorithm using vertex as opposed to multiscale asymptotes, the two solutions ultimately converge once the transients have decayed. This analysis thus establishes the important result that, unless the purpose of the modelling is to provide a smooth solution with great detail around the arrest–recession transition point t_r, a pragmatic, and much more efficient approach, is to use a simpler algorithm based solely on vertex asymptotes.

We perform a scaling analysis in terms of the dimensionless shut-in time ω and the dimensionless arrest regime parameter ϕ^V that is able to capture the power law dependence of the arrest time, the arrest radius, and the arrest aperture on ω. In contrast to the analysis of Mori and Lecampion (2021), this novel parameterization maintains the same power law relationships for both the zero and finite fracture toughness cases. We also establish the first scaling law for the deflation time, which also has a unified power law for both the zero and finite fracture toughness cases. All these power law relationships are confirmed using a numerical scheme that includes the arrest–recession multiscale tip solution, which was established using rigorous asymptotic analysis.

Using this scheme, we explore the impact that changes in the dimensionless parameters ω and ϕ^V have on the time between shut-in and arrest, the duration of arrest, and the elapsed time from the initiation of arrest to collapse of the fracture. For fixed ϕ^V, the ratio t_c/t_s between the collapse time and the shut-in time decreases as the dimensionless shut-in time ω increases. For fixed ω, the proportion of time spent deflating while the fracture has arrested decreases as ϕ^V increases, while the proportion of time spent solely on recession remains almost constant. We also provide estimates of the range of dimensionless parameters ω and ϕ^V one could expect if a realistic range of the material and injection parameters encountered in the field are used. For values of the input parameters that are within the range one might encounter in the field, we also provide the post shut-in solution in physical units for a radial hydraulic fracture that propagates after shut-in, deflates during arrest, and recedes till collapse.

Data

The data used to generate the plots in Table 1 and Fig. 6 are available for download (Peirce, 2022).

Declaration of competing interest

The authors declare that they have no known competing financial interests or personal relationships that could have appeared to influence the work reported in this paper.

Acknowledgements

The author would like to thank Prof.E. Detournay (University of Minnesota) for many insightful discussions and comments throughout the development of this research project.

Funding

The author acknowledges the support of the British Columbia Oil and Gas Commission and the discovery grants program of the Natural Sciences and Engineering Research Council of Canada (NSERC) (grant number RGPIN-2015-06039) for funding this research.

References

Adachi, J.I., Detournay, E., 2008. Plane-strain propagation of a fluid-driven fracture in a permeable medium. Engrg. Fract. Mech. 75, 4666–4694.
Adachi, J., Siebrits, E., Peirce, A., Desroches, J., 2007. Computer simulation of hydraulic fractures. Int. J. Rock Mech. & Min. Sci. 44, 739–757.
Bunger, A.P., Detournay, E., 2008. Experimental validation of the tip asymptotics for a fluid-driven crack. J. Mech. Phys. Solids 56, 3101–3115.
Carter, E.D., 1957. Optimum fluid characteristics for fracture extension. In: Howard, G.C., Fast, C.R. (Eds.), Drilling and Production Practices. American Petroleum Institute, Tulsa, OK, pp. 261–270.
van Dam, D.B., de Pater, C.J., Romijn, R., 2000. Analysis of hydraulic fracture closure in laboratory experiments. SPE Prod. Facilit. 15 (03), 151–158.
De Pater, H., Desroches, J., Groenenboom, J., Weijers, L., 1996. Physical and numerical modeling of hydraulic fracture closure. SPE Prod. Facilit. 11 (02), 122–128.
Desroches, J., Detournay, E., Lenoach, B., Papanastasiou, P., Pearson, J.R.A., Thiercelin, M., Cheng, A.H.D., 1994. The Crack Tip Region in hydraulic fracturing. Proc. R. Soc. Lond. Ser. A Math. Phys. Eng. Sci. 447, 39–48.
Desroches, J., Thiercelin, M., 1993. Modelling the propagation and closure of microhydraulic fractures. Int. J. Rock Mech. Min. Sci. 30 (7), 1231–1234.
Detournay, E., 2004. Propagation regimes of fluid-driven fractures in impermeable rocks. Int. J. Geomech. 4 (1), 1–11.
Detournay, E., 2016. Mechanics of hydraulic fractures. Annu. Rev. Fluid Mech. 48, 311–339.
Detournay, E., Peirce, A., 2014. On the moving boundary conditions for a hydraulic fracture. Internat. J. Engrg. Sci. 84, 147–155.
Dontsov, E.V., 2016. An approximate solution for a penny-shaped hydraulic fracture that accounts for fracture toughness, fluid viscosity and leak-off. R. Soc. Open Sci. 3, 160737.
Dontsov, E.V., 2017. An approximate solution for a plane strain hydraulic fracture that accounts for fracture toughness, fluid viscosity, and leak-off. Int. J. Fract. 205, 221–237.
Dontsov, E., Peirce, A., 2015. A non-singular integral equation formulation to analyse multiscale behaviour in semi-infnite hydraulic fractures. J. Fluid Mech. (JFM RAPIDS) 781 (R1).

Dontsov, E.V., Peirce, A., 2017. A multiscale implicit level set algorithm (ILSA) to model hydraulic fracture propagation incorporating combined viscous, toughness, and leak-off asymptotics. Comp. Meth. Appl. Mech. and Eng. 313, 53–84.

Economides, M.J., Nolte, K.G., 2000. Reservoir Stimulation. John Wiley & Sons.

Garagash, D.I., 2006. Plane-strain propagation of a fluid-driven fracture during injection and shut-in: Asymptotics of large toughness. Engrg. Fract. Mech. 73, 456–481.

Garagash, D.I., Detournay, E., 2000. The tip region of a fluid-friven fracture in an elastic medium. ASME J. Appl. Mech. 67 (1), 183–192.

Garagash, D.I., Detournay, E., Adachi, J.I., 2011. Multiscale tip asymptotics in hydraulic fracture with leak-off. J. Fluid Mech. 669, 260–297.

Hills, D.A., Kelly, P.A., Dai, D.N., Korsunsky, A.M., 1996. Solution of Crack Problems, the Distributed Dislocation Technique, Solid Mechanics and its Applications, Vol. 44. Kluwer Academic Publisher, Dordrecht.

Khristianovic, S.A., Zheltov, Y.P., 1955. Formation of vertical fractures by means of highly viscous fluids. In: Proc. 4th World Petroleum Congress, Vol. 2, pp. 579–586.

Lecampion, B., Peirce, A., Detournay, E., Zhang, X., Chen, Z., Bunger, A., Detournay, C., Napier, J., Abbas, S., Garagash, D., Cundall, P., 2013. The impact of the near-tip logic on the accuracy and convergence rate of hydraulic fracture simulators compared to reference solutions. In: Effective and Sustainable Hydraulic Fracturing. InTech, ISBN: 978-953-51-1137-5, http://dx.doi.org/10.5772/45724, Chapter 43.

Madyarova, M., 2003. Fluid-Driven Penny-Shaped Fracture in Permeable Rock (M.Sc. Thesis). University of Minnesota.

McClure, M.W., Horne, R.N., 2013. Discrete Fracture Network Modeling of Hydraulic Stimulation: Coupling Flow and Geomechanics. SpringerBriefs in EarthSciences, Springer.

Mohammadnejad, T., Andrade, J.E., 2016. Numerical modeling of hydraulic fracture propagation, closure and reopening using XFEM with application to in-situ stress estimation. Int. J. Numer. Anal. Methods Geomech. 40 (15), 2033–2060.

Mori, A., Lecampion, B., 2021. Arrest of a radial hydraulic fracture upon shut-in of the injection. Int. J. Solids Struct. 219–220, 120–133.

Nolte, K.G., 1979. Determination of fracture parameters from fracturing pressure decline. In: Proc. SPE Ann. Tech. Conf. & Exhib.. SPE 8341, Las Vegas.

Peirce, A., 2015. Modeling multi-scale processes in hydraulic fracture propagation using the implicit level set algorithm. Comp. Meth. Appl. Mech. Eng. 283, 881–908.

Peirce, A., 2016. Implicit level set algorithms for modelling hydraulic fracture propagation. Phil. Trans. R. Soc. A 374, 20150423.

Peirce, A., 2022. Post shut-in arrest and recession solutions for a deflating hydraulic fracture in a permeable elastic medium. Mendeley Data, v1 http://dx.doi.org/10.17632/4nxghz7cmr.1.

Peirce, A., Detournay, E., 2008. An implicit level set method for modeling hydraulically driven fractures. Comp. Meth. Appl. Mech. Eng. 197, 2858–2885.

Peirce, A., Detournay, E., 2022a. Multiscale tip asymptotics for a deflating hydraulic fracture with leak-off. J. Fluid Mech. submitted.

Peirce, A., Detournay, E., 2022b. Sunset similarity solution for a receding hydraulic fracture. J. Fluid Mech http://dx.doi.org/10.1017/jfm.2022.430, in press.

Rice, J.R., 1968. In: Liebowitz, H. (Ed.), Mathematical Analysis in the Mechanics of Fracture, Fracture, an Advanced Treatise. Academic Press, New York, pp. 191–311, Chap. 3.

Savitski, A., Detournay, E., 2002. Propagation of a fluid-driven penny-shaped fracture in an impermeable rock: asymptotic solutions. Int. J. Solids Struct 39, 6311–6337.

Spence, D.A., Sharp, P., 1985. Self-similar solutions for elastohydrodynamic cavity flow. Proc. R. Soc. Lond. Ser. A Math. Phys. Eng. Sci. 400, 289–313.

Zanganeh, B., Clarkson, C.R., Hawkes, R.V., 2017. Reinterpretation of fracture closure dynamics during diagnostic fracture injection tests. In: Proc. SPE Ann. Tech. Conf. & Exhib. the Woodlands. Texas, SPE-189840-MS.